AXIS White Paper

Prospects for Compact Objects and Supernova Remnants Studies with AXIS

Firstname Lastname [1,†], Firstname Lastname [1] and Firstname Lastname [2]

[1] Affiliation 1; e-mail@e-mail.com
[2] Affiliation 2; e-mail@e-mail.com
† Current address: Affiliation 3

Abstract: Compact objects (CO) and Supernova Remnants (SNRs) provide nearby laboratories to probe the fate of stars after they die, and the way they impact, and are impacted by, their surrounding medium. The past five decades have significantly advanced our understanding of these objects, and showed that they are most relevant to our understanding of some of the most mysterious energetic events in the distant Universe, including Fast Radio Bursts and Gravitational Wave sources. However, many questions remain to be answered. These include: What powers the diversity of explosive phenomena across the electromagnetic spectrum? What are the mass and spin distributions of neutron stars and stellar mass black holes? How do interacting compact binaries with white dwarfs - the electromagnetic counterparts to gravitational wave LISA sources - form and behave? Which objects inhabit the faint end of the X-ray luminosity function? How do relativistic winds impact their surroundings? What do neutron star kicks reveal about fundamental physics and supernova explosions? How do supernova remnant shocks impact cosmic magnetism? This plethora of questions will be addressed with AXIS - the Advanced X-ray Imaging Satellite - a NASA Probe Mission Concept designed to be the premier high-angular resolution X-ray mission for the next decade. AXIS, thanks to its combined (a) unprecedented imaging resolution over its full field of view, (b) unprecedented sensitivity to faint objects due to its large effective area and low background, and (c) rapid response capability, will provide a giant leap in discovering and identifying populations of compact objects (isolated and binaries), particularly in crowded regions such as globular clusters and the Galactic Center, while addressing science questions and priorities of the US Decadal Survey for Astronomy and Astrophysics (Astro2020).
This White Paper is part of a series commissioned for the AXIS Probe Concept Mission; additional AXIS White Papers can be found at [some url].

---

1. Introduction

Currently, the white paper is organized in terms of topics, but we should **preface each of these sections with the big science question to answer**, e.g. 'Using AXIS to unveil the progenitors of SNRs' and tie it to Astro2020 theme/science. Some merging of topics or text may happen later.

2. Galactic Plane Survey

The inner quadrant of the Milky Way is densely packed with massive stars residing among the wide lanes of obscuring gas and dust that form the spiral arms. When a massive star goes supernova (SN), its core forms a compact object (CO) such as a neutron star (NS) or a black hole (BH). Low-mass stars like the Sun end their lives as a planetary nebula where the outer layers are shed leaving behind a white

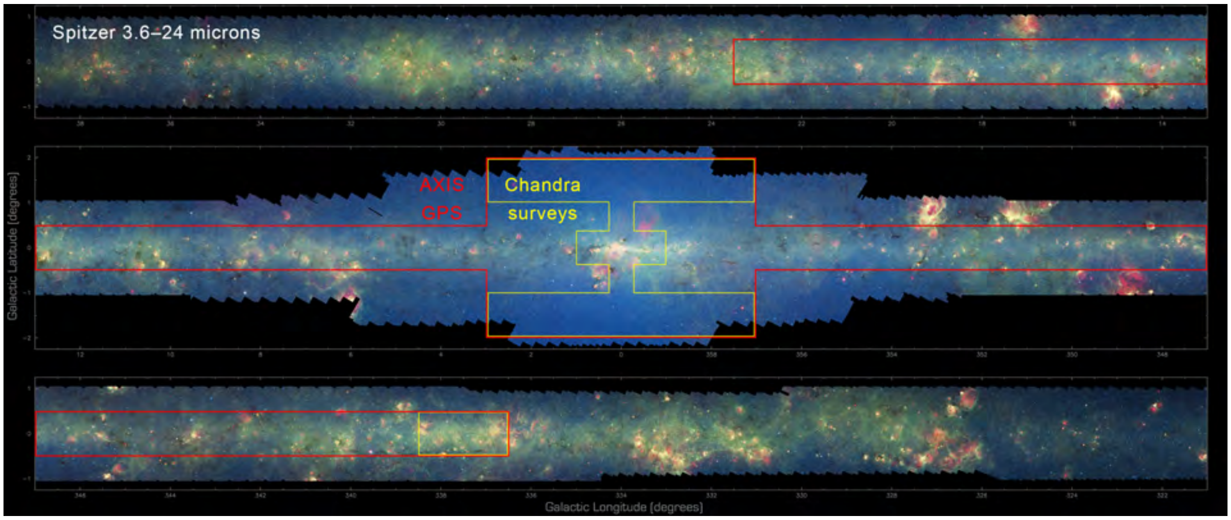

Figure 1. *Spitzer*-GLIMPSE/MIPSGAL image combining 3.6, 8, and 24 μm infrared wavelengths [52] overlaid with the outlines of the *AXIS* GPS footprint in red and some existing *Chandra* surveys in yellow.

dwarf (WD). Thus, the inner galactic plane hosts the greatest concentration of systems with COs, e.g., X-ray binaries (XRBs) with low-mass or high-mass stellar companions (LMXBs and HMXBs, respectively), cataclysmic variables (CVs), ultra-compact WD binaries, rotation-powered pulsars (RPPs), pulsar and magnetar wind nebulae (PWNe and MWNe), and supernova remnants (SNRs). X-ray photons from these systems are messengers of matter subject to extreme gravitational and electromagnetic fields. In addition, some of these systems could form inspiraling binaries which are precursors to the types of gravitational wave events detectable by LIGO/Virgo, and eventually, *LISA* [e.g., 4,178,221].

X-ray surveys by *Chandra* detected 9017 sources in a $2^\circ \times 0.8^\circ$ section of the galactic center [205]. The deepest exposures ($\sim$1 Ms) were centered on Sgr A* where the source density approached 10 sources per arcmin^2 with a minimum luminosity of $L \geq 3 \times 10^{31}$ erg s^{-1} in the 0.5–8 keV energy range. A similar survey of the Norma Arm uncovered 1415 sources [82], while a shallower, but wider ($2 \times 6^\circ \times 1^\circ$), survey of the galactic bulge found 1640 sources [144]. The central parsecs around Sgr A* includes sources with non-thermal spectra distinct from the thermal spectra of active binaries (ABs), dwarf novae (DNe), and non-magnetic CVs that are the dominant X-ray populations in the center, bulge, and plane. Among these, at least 6 NS-LMXB systems and 18 BH-LMXB candidates have been proposed [e.g., 171,196]. Their spatial distribution and luminosity function suggest a population of hundreds of quiescent BH- and NS-LMXBs, with decades-long periods of inactivity, lurking below the *Chandra* sensitivity limit [91,111].

In addition to these point sources, the inner galaxy contains large-scale diffuse background emission in the X-rays and gamma-rays: e.g., the hot gas surrounding Sgr A* [e.g., 202]; the Galactic Chimneys [238]; the Fermi Bubbles [e.g., 284] and GeV excess [e.g., 5]; the 511-keV line from positron annihilation [e.g., 270,271]; and the Galactic Ridge X-ray Emission [GRXE: e.g., 253]. In some cases, the diffuse emission is the result of the combined emission from different populations of resolved and unresolved point sources, each with its own luminosity range and continuum temperature. For example, $\sim$80% of the GRXE around 6–8 keV can be attributed to thousands of accreting WDs such as CVs and DNe [e.g., 64,224,252,311,323]. Faint, coronally-active stars and ABs are believed to produce the low-temperature emission around 1 keV [e.g., 327], while the more luminous population of magnetic CVs [132] and intermediate-polar CVs [113] may explain the emission seen around 15 keV [293,327]. Rotation-powered pulsars (RPPs) are predicted to be present in significant numbers in the galactic center and could be responsible for the GeV excess [5], and possibly, in combination with flaring stars and XRBs, the origin of the 511-keV signal as well

[271]. However, only one such object is known within 20 pc of Sgr A*: the Cannonball Pulsar. The lack of RPPs in the galactic center is puzzling, though simulations show that pulsars can be rapidly ejected from their birthplace due to natal kicks [33]. Additionally, the Galactic Center environment encourages the production of magnetars, instead of normal-B neutron stars, and so the NS population could include a large fraction of magnetars [69]. The detection of the missing magnetar and pulsar population in the central regions of the galaxy, in addition to the first discovered magnetar (SGR J1745–2900, $\sim$2.4$''$ away from Sgr A*) and the Cannonball pulsar, would shed light on this hidden population's abundance (i.e., how massive stars evolve) and distribution (i.e., the energetics of SNe).

Therefore, the primary science question is: **which X-ray populations inhabit the faint end of the X-ray luminosity function and how do they contribute to the diffuse X-ray and gamma-ray background?** Unfortunately, a census of the different X-ray populations that occupy the inner galaxy is incomplete. Existing *Chandra* and *XMM-Newton* surveys form a relatively small patchwork of images with exposure times that are not uniform, the limiting sensitivity of the Bulge was sacrificed in favor of wider field coverage making the survey biased towards bright X-ray populations, and some of the bulge and almost all of the inner disk remains unmapped. The *Chandra* field-of-view (FoV) is narrow which makes mapping a large area impractical. *XMM-Newton* has a wider FoV but its point-spread-function (PSF) is large which hinders the resolving of individual point sources in dense fields. In both of these instruments, the PSF broadens for sources located off axis. Relating the X-ray source to a counterpart at lower energies is crucial for determining which class of system is involved. While telescopes operating in the radio, infrared, and optical bands feature astrometric precision of a few tenths of an arcsec, X-ray sources are typically discovered with position uncertainties of a few arcsec to a few arcmin. Given the stellar density in the plane, and especially the center, such wide X-ray error circles encompass several dozen candidates, any one of which could be the low-energy counterpart.

The *AXIS* Galactic Plane Survey (GPS: Fig. 1) will cover a 62-deg^2 swath of the sky centered on the GC extending to longitudes of $\pm$23.5 deg, i.e., from the Scutum/Sagittarius Arm to the Inner/Norma Arm, with latitudes of $\pm$0.5 deg ($\pm$2 deg in the Bulge). Its wide FoV and narrow PSF make *AXIS* perfectly suited for creating a wide-field census of the Milky Way's X-ray populations. These observations represent a legacy-level dataset that will complement existing surveys in other wavelengths, as well as overlap with planned surveys from the Roman and Rubin observatories, and it will serve in the study of all X-ray source classes. The total exposure time is approximately 4 Ms which is comparable to that of all *Chandra* surveys of this region thus far (3.5 Ms). A minimum of 5 ks of exposure is allocated to each location so that the limiting flux (0.5–10 keV) for a source detected at significance of 5σ is 3×10^{-15} erg cm^{-2} s^{-1} assuming a power-law spectrum with 2×10^{22} cm^{-2} and $\Gamma = 1.5$. In the GC, where the planned exposure times are 50 ks to 250 ks, the flux limits will be 10^{-15} erg cm^{-2} s^{-1} and 10^{-16} erg cm^{-2} s^{-1}, respectively, which correspond to luminosities of 10^{31} erg s^{-1} and 10^{30} erg s^{-1} for a distance of 8 kpc. This means **the GPS will be the most sensitive, high-resolution X-ray map of the galactic plane ever made with a flux limit 1–2 orders of magnitude below those of *Chandra* and *XMM-Newton***.

Figure 3 presents a simulated 100-ks *AXIS* observation of the galactic center compared with a 167-ks *Chandra* observation of the same field. Figure 4 presents simulated images and flux distributions for sources in a typical region of the galactic bulge. Exposure times of 5 ks, 50 ks, and 250 ks, respectively, will enable the detection of 9%, 45%, and 85% of the faint, unresolved X-ray population in the plane, bulge, and center. For the plane, bulge, and center, respectively, extrapolation of the *Chandra* log$N$-log$S$ curve [205] with slopes of -1.0, -1.3, and -1.5 to these lower flux limits yields source densities of 3.6×10^4, 1.5×10^5, and 3×10^6 sources deg^{-2}. Within the GPS footprint, over 1 million sources are expected to be discovered along with the re-detection of 35,000–50,000 sources listed in the serendipitous survey catalogs of *Chandra* and *XMM-Newton*. In the center, all known CVs and XRBs with a distance less than 20 kpc will be detected, as well as heretofore undetected populations of faint CVs and quiescent LMXBs out

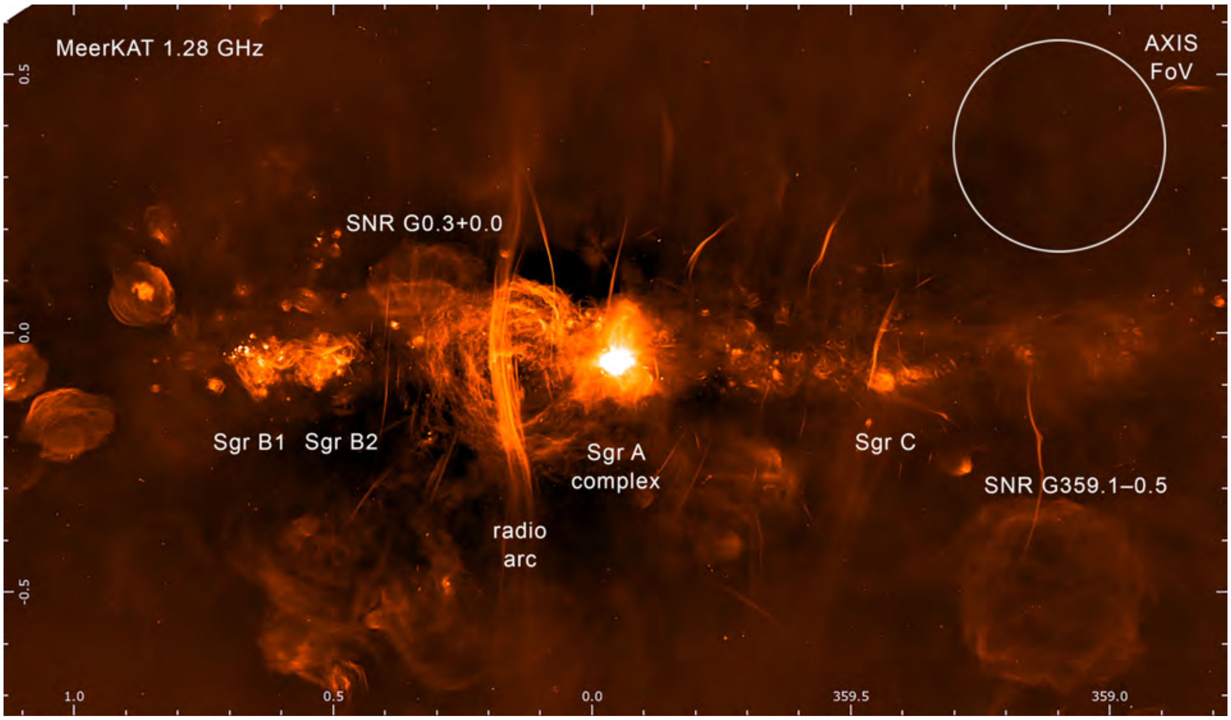

Figure 2. MeerKAT image in 1.28 GHz showing the complex structure of the diffuse radio emission in the GC [125]. The size of the *AXIS* field-of-view is shown as a white circle in the upper right. This field will be fully mapped by the *AXIS* GPS down to a flux limit of 10^{31} erg s^{-1} for 90% of the field, and 10^{30} erg s^{-1} near Sgr A*.

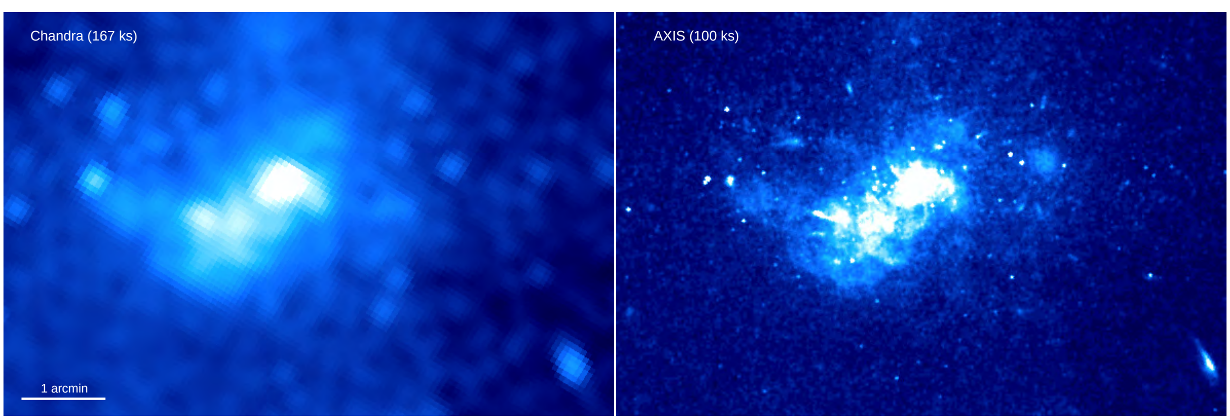

Figure 3. The left panel shows the *Chandra* image (ObsID 3392; 167 ks) of the vicinity of Sgr A* and the right panel presents a simulated *AXIS* image of the same region (100 ks). Both images are given in galactic coordinates in the 0.5–10 keV energy range, with logarithmic scaling and Gaussian smoothing. One arcmin is equivalent to 2.3 pc at the galactic center distance of 8 kpc.

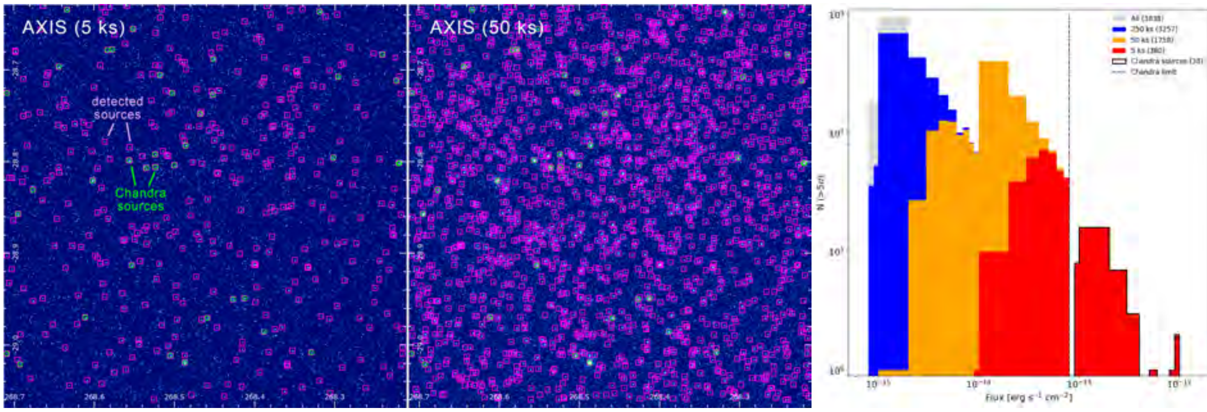

Figure 4. Simulated *AXIS* image in 0.5–10 keV for a representative section of the galactic bulge centered at $(l;b) = (+1.0; -1.5)$ with 5 ks and 50 ks of exposure time (two left-most panels). In addition to the 38 *Chandra* sources (circled in green) within the *AXIS* FoV whose fluxes are known [144], the simulation included 3,800 faint, uniformly-distributed mock sources. All sources were assigned an absorbed power-law spectrum ($N_{\mathrm{H}} = 2 \times 10^{22}$ cm^{-2}; Γ=1.5) with mock sources given fluxes ranging from the Chandra sensitivity limit of 8×10^{-14} down to 8×10^{-16} erg cm^{-2} s^{-1} according to a log$N$–log$S$ curve with $\alpha = 1.3$. Magenta squares denote sources detected above 5σ significance. The right panel shows the flux distribution of detected sources (with numbers in parentheses) for typical exposure times of the GPS. The *Chandra* flux distribution and sensitivity limit are indicated by the thick and dashed lines, respectively.

to 9 kpc. In the bulge and plane, the known population of persistent and active-transient XRBs will be detected through the galaxy while many transient systems in quiescence will be observable to a distance of 4–8 kpc. A detection significance of 5σ ensures that even if most sources emit only a handful of counts, they will have an X-ray position with an error radius on the order of an arcsec which, in all but a small minority of cases, is constricting enough to exclude all but 1 or 2 counterpart candidates. Optical/infrared spectroscopy of these candidates, along with basic X-ray timing and spectral information from the GPS observation or from deeper follow-up observations with other telescopes, will help categorize the object into one of the source classes. The data will be valuable for studies of diffuse emission beyond the link with point sources: the regions covered include where the Galactic Chimneys meet the Fermi Bubbles, the peak and possible asymmetric profile of the positron annihilation signal, and the molecular clouds and filamentary structures highlighted in recent radio maps by MeerKAT [125]. The tight PSF and low detector background of *AXIS* are ideal for X-ray imaging and spectral analysis of faint, diffuse structures allowing a broad-band study of these features from radio to X-rays (Fig. 2).

Which CO populations inhabit the faint end of the X-ray luminosity function and how do they contribute to diffuse emission? The *AXIS* GPS will reveal a crowd of X-ray sources hidden in the background of previous surveys of the Milky Way, which will clarify the origin of different types of diffuse emission: e.g., point-vs.-diffuse emission in the vicinity of Sgr A*; pulsars and the 511-keV line; ABs/CVs and the GRXE; and the Fermi Bubbles. All source classes are expected in the GPS, including extragalactic sources, SNRs, and the precursors to GW events, so the GPS data will hold legacy value by complementing and expanding on past (*Spitzer*), present (*Chandra*, *eRosita*), and future (*Rubin*, *Roman*) multi-wavelength surveys.

What can AXIS measure? The GPS represents a sky area of 62 deg^2, inside of which *AXIS* will detect around 1 million new objects with (sub-)arcesec error radii. In the crowded fields of the Galactic Plane and Center, an error radius smaller than an arcsec is required to identify the likely optical/IR counterparts. Along with the multi-wavelength counterparts, *AXIS* will also provide spectral and timing information helping to narrow down the class to which each source belongs. Thanks its low detector background, *AXIS* will map the low-surface brightness diffuse emission with a better sensitivity and spatial resolution than previously possible enabling the location (hence, the energetics and dynamics) of sources responsible for accelerating particles that lead to diffuse emission like the GRXE or positron annihilation signatures, as well as outflows such as the Galactic Chimneys and Fermi Bubbles.

How will AXIS measure it? Simulations show that an exposure time of 5 ks (250 ks) enables a sensitivity limit of 10^{-15} (10^{-16}) erg cm^{-2} s^{-1}. This would represent 1—2 orders of magnitude below previous surveys in 0.5—10 keV despite having equal or less exposure. *AXIS* is ideal for imaging crowded X-ray populations and diffuse emission thanks to its angular resolution and imaging/spectral sensitivity over a wide FoV. The GPS plays to these qualities with a large survey area and a uniform exposure. Once *AXIS* constrains the emission from point sources within its narrow PSF, and has defined their SEDs, the residual diffuse emission can be studied in unprecedented detail.

The GPS addresses several science questions posed by the Astro2020 Decadal Survey [208]:

- What is the population of non-interacting or isolated NSs and stellar-mass BHs? (B-Q1b)
- What powers the diversity of explosive phenomena across the electromagnetic spectrum? (B-Q2)
- Why do some compact objects eject material in nearly light-speed jets, and what is that material made of? (B-Q3)
- What are the endpoints of stellar evolution?
- What are the progenitors and explosion mechanisms of supernovae? (COEP2)
- How do relativistic winds and jets interact with and energize the surrounding medium? (COEP3)
- What are the most extreme stars and stellar populations? (G-Q1)
- How does multiplicity affect the way a star lives and dies? (G-Q2)

Many of these questions can be answered by creating a census of X-ray populations that represent the final stages in the lives of stars. This is especially true for the faint end of each population's luminosity function where *AXIS*, thanks to its low detector background and high spatial resolution, will detect X-ray sources too dim to be seen by other telescopes. In addition to accessing the faint end of the X-ray luminosity function for compact objects, AXIS will also allow us to discover younger, high-energy diffuse sources associated with the explosive outcomes of stellar evolution, namely SNRs, PWNe and MWNe. Studying these objects helps us address the question on what happens to stars after they die, sheds light on the explosion mechanisms and progenitors of SNe, and reveals extreme particle accelerators in the Universe. *Chandra* and *XMM-Newton* have opened a new window to linking SNRs to their progenitors, revealing a zoo of neutron stars and associated outflows, and showing pulsar winds as powerful cosmic accelerators of positrons up to PeV energies. However, given *Chandra*'s restricted FoV and its sensitivity degradation, it cannot be used effectively as a survey instrument which essentially results in a bias towards the brighter population. On the other hand the *XMM-Newton* background is too high preventing the detection of faint and extended sources, or limiting our ability to resolve compact Pulsar or Magnetar Wind Nebulae. Therefore, there remains a significant discovery space for *AXIS* in terms of endpoints of stellar evolution and death, which will be enabled by the unique large area and high sensitivity to be achieved with the GPS.

The following sections detail how *AXIS* will help answer these questions.

2.1. Ultra Compact White Dwarf Binaries

Type Ia supernovae are important standard candles that arise from the explosion of a white dwarf. There has been significant debate over the years as to the physical mechanism underlying these important explosive transients, with two main progenitor scenarios, the single-degenerate channel in which a white dwarf accretes matter from a non-degenerate object and then explodes, or the double degenerate channel, originating from the interaction of two white dwarfs. The rate of type Ia supernovae in the Milky Way is $\approx 0.3 \times 10^{-2}$ yr^{-1}, and it is estimated that the white dwarf merger rate is approximately $4.5 - 7$ times this [184]. When a double white dwarf system starts to undergo Roche-lobe overflow, it can undergo a unique form of accretion known as direct impact accretion, in which the accretion stream directly impacts the surface of the more massive white dwarf rather than forming an accretion disk, resulting in significant X-ray emission, and strong periodic modulation of these X-rays. For merging double white dwarfs with close to equal mass ratio (e.g. a 0.6 $M_\odot$ plus a 0.8 $M_\odot$ white dwarf), this phase is short-lived, as the lower mass white dwarf is so dense that it does not undergo Roche lobe overflow until an orbital period of just 40 seconds, at which point the gravitational wave merger timescale is only $\sim 10^2$ yr. If all type Ias originated from this channel, we would only expect ~ 1 such accreting system to exist in the Galaxy at any given time. However, recent work has indicated that it is far more likely that most Type Ia supernovae originating from double degenerate progenitors likely arise from lower mass helium core white dwarfs accreting onto more massive carbon-oxygen core companions, in many cases via physical mechanisms such as the dynamically driven double degenerate double detonations (D6) [266]. Such systems can undergo Roche-lobe overflow at orbital periods of > 5 minutes, with gravitational wave merger timescales of $\approx 10^5$ yr, suggesting that $\approx 10^3 - 10^4$ such systems might exist in the Galaxy, including dozens which might trigger supernovae in the future. Additionally, many of these systems undergo stable mass transfer and become AM CVn-type binaries, and recent work with the Zwicky Transient facility has demonstrated the existence of many new eclipsing AM CVns with ultrashort orbital periods (Burdge et al., in prep). With the 60 square-degree AXIS Galactic plane survey at a depth of $\sim 10^{-15}$ ergs^{-1}, we expect to be sensitive to disk-dominated systems such as the recently discovered ZTF J0127+5242 at a distance of ~ 8 kpc, allowing us to probe approximately ~ 5 percent of such systems in the Galaxy. We include a portion of the relatively unobscured Bulge region in our footprint to maintain sensitivity to direct impact accreting systems such as HM Cancri, which have very soft spectra and are easily obscured. We estimate that at a column density of $n_H = 2 \times 10^{21}$, we would be able to blindly detect a source like HM Cancri in periodicity search at a distance of $>$ 20kpc in a 5 kilosecond AXIS exposure. Current estimates indicate that 2×10^{10} $M_\odot$ of stellar mass resides in the Galactic Bulge [296], and 5.17×10^{10} $M_\odot$ in the disk[175], indicating that the Bulge hosts approximately 28 percent of the stars in the Galaxy. These stars are distributed over approximately 380 square degrees, which means the stellar density is high enough such that each square degree contains approximately 0.073 percent of stars in the Galaxy. Thus, by including 78 square degrees of relatively unobscured regions of the Bulge in the AXIS GPS survey, we will systematically probe around 5.7 percent of stars in the Milky Way for direct impact accretors. If there are 1000 direct impact accretors in the Galaxy, we expect 60.00 ± 7.75 direct impact systems to reside in this 80 sq degree footprint in the Bulge. Assuming we can confidently detect half of these systems (since approximately half should undergo full x-ray eclipses) if we do not detect any systems and they trace the stellar mass of the Galaxy, we will have ruled out there being more than 320 such systems in the Galaxy with 3σ confidence (e.g if there are 320 such systems in the Galaxy evenly distributed among the stellar mass, the probability of our search identifying zero of them given that half are eclipsing is 0.0003). Given the rate of inspiraling double degenerates, we estimate that in our full survey footprint we will be able to detect approximately 30 pre-period minimum mass-transferring ultracompact binaries including direct impact systems and disk-dominated systems such as ZTF J0127+5242 (and an additional 30 eclipsing post-period minimum AM CVn objects such as the recently discovered 55 minute eclipsing AM CVn in the SRG eFEDs field). We plan to leverage the five-year baseline of the survey to measure orbital evolution in any detected systems to determine whether they are inspiraling and are likely to merge/trigger a supernova, or are undergoing stable mass transfer and likely to evolve into an AM CVn type system.

Our efforts are inspired by the shortest orbital period binary known in the Galaxy, HM Cancri (orbital period 5.35 minutes), which is a direct impact accreting system that was discovered using the ROSAT all-sky survey because it strongly modulates its X-ray flux on its orbital period. In this remarkable system,

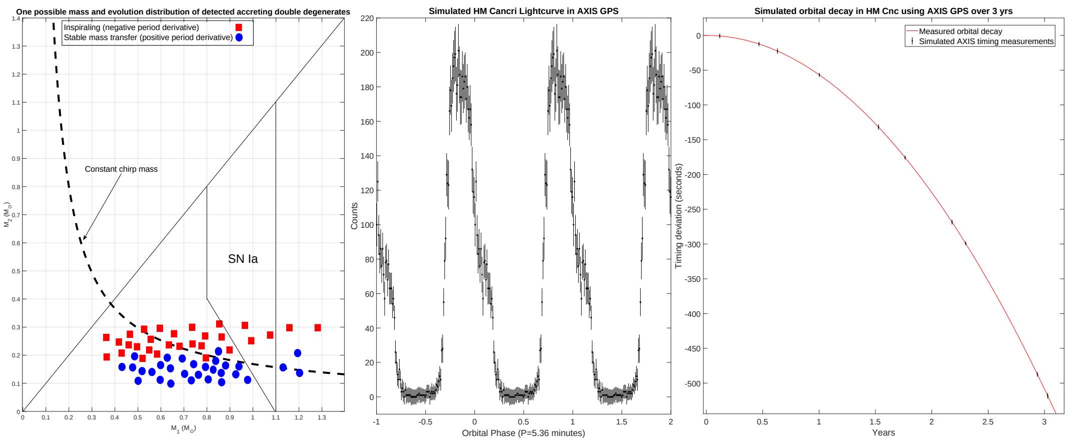

Figure 5. .

the hot spot on the accreting white dwarf is eclipsed every orbit of the binary, leading to a 100 percent modulation of the X-ray flux, as shown in Figure XX. Long-term timing of the X-ray waveform has also revealed strong orbital decay due to the emission of gravitational radiation, and remarkably, has led to a measurement of the second derivative of the orbital frequency, which indicates that the mass transfer in the binary is counteracting the angular momentum loss due to GR and is slowing down the decay rate and that the system should reach a minimum orbital period in just a few thousand years. One can use the masses inferred from this orbital evolution to conclude that HM Cancri is unlikely to be a type Ia progenitor, and will instead likely transition to stable mass transfer. This source illustrates how a sensitive X-ray time domain survey can be used both to identify ultracompact binaries, and via timing measurements, characterize the chirp mass of the system, and thus whether it is likely to be a Type Ia supernova progenitor. By using AXIS to conduct a survey of the Galactic Plane, we will leverage its sharp PSF over a wide field of view to create the highest spatial resolution X-ray map of the Galactic plane, and its effective area will allow us to collect enough spatially resolved photons with cadenced temporal resolution so that we can use periodicity analyses on these x-ray sources to discover sixty new interacting ultracompact binaries detectable in the LISA band. Using the five-year baseline of the survey, we will measure orbital evolution in these systems (as seen in panel b of Figure XX) to determine whether they are likely to result in a type Ia supernova. By discovering 60 such systems, we can confirm or rule out whether more than a few percent of the interacting double degenerate population in our Galaxy are likely to result in Type Ia supernovae. Additionally, by measuring which systems are undergoing stable mass transfer and evolving out to longer orbital periods, we may be able to constrain which combinations of white dwarf masses lead to merger and explosion, and which lead to stable mass transfer.

2.2. Population Studies from the proposed GPS

2.2.1. Machine Learning Classification

With AXIS's sufficient sensitivity, large FOV, and excellent PSF, we will be able to detect many more (probably millions of) X-ray sources with arcsecond localizations, from the surveys like the GPS, compared to previous and existing observatories (e.g., Chandra). In such an era of large data astronomy, rapid classification of a huge number of sources becomes a particularly important task. New software and methods have been developed, to enable cross-matching sources from different surveys and catalogs [260], and to apply on-the-fly classification of X-ray sources using methods like machine learning (ML) [292,324]. Among those, a multiwavelength machine learning pipeline for classification of X-ray sources

(MUWCLASS) [324] has been developed by colleagues from our CO/SNR science group. The major component of a supervised ML pipeline is the training dataset (TD), which is a collection of sources with confident classifications. In MUWCLASS, there are several thousands of X-ray sources in the TD which are categorized into 8 classes of X-ray emitters including active galactic nuclei (AGNs), cataclysmic variables, high-mass stars, HMXBs, low-mass stars, LMXBs, NSs, and young stellar objects. AXIS will accurately measure the X-ray energy fluxes at multiple energy bands, the X-ray hardness ratios, and the X-ray variability properties of each X-ray sources, given its high sensitivity and the relatively good timing resolution (of $\sim 0.2\,$s or even better). Besides the X-ray features, the photometric properties (e.g., magnitudes and colors) at lower frequencies are also crucial to ML classifications to break the degeneracy of classifications when using only the X-ray properties. The sub-arcsecond localizations from AXIS observations make it possible to enable accurate cross-correlating between the X-ray sources and multiwavelength surveys at lower frequency, especially in a crowded environment like the GPS.

MUWCLASS is trained with an supervised ensemble decision-tree algorithm called random forest. To mitigate the bias of the extinction/absorption of AGNs from the TD which come from surveys conducted away from the Galactic plane, MUWCLASS applies location-specific reddening/absorption corrections to AGNs from the TD while classifying sources in the Galactic plane. It also uses an implementation of the synthetic minority over-sampling technique to oversample the TD [46] to overcome the large imbalance of source types from the TD. Measurement uncertainties are also taken into account by Monte Carlo (MC) sampling from feature probability density functions and averaging multiple MC sampling results to obtain confident classifications and measure their uncertainties. The performance of MUWCLASS has an overall accuracy of about 86%, up to 95% for confident classifications.

Moderate-resolution CCD X-ray spectra, by themselves, can also be used to distinguish different kinds of X-ray sources. Chromospherically active stars emit strong Fe-L and Ne-K lines (~ 1 keV), and SNRs have dominant Mg-K (~ 1.3 keV) and Si-K (~ 1.8 keV) line emissions. The X-ray spectra of NS and AGN are not line-dominated (though AGN can also have a fluorescent Fe line at rest energy of 6.4 keV). Thus, ML algorithms that can distinguish between line-dominated and continuum-dominated sources can separate X-ray sources from their X-ray spectra alone. Such methods can either be used as stand-alone classification algorithms when multi-wavelength observations and cross-matching are not feasible, or in combination with other multi-wavelength classification algorithms. Hebbar & Heinke [119] tested this idea by using an artificial neural network (ANN) to differentiate the *Chandra* spectra of stars in the Chandra Orion Ultradeep Project (COUP) from the spectra of AGN in the Chandra Deep Field South (CDFS) catalog and separated the two classes with an overall accuracy of 90%. Their results found that the accuracy of the ANN classification is greater than 90% for sources with net counts greater than 200 and background contribution less than 5%. For a 100 ks *Chandra* exposure, this implies that we can accurately ($> 90\%$ confidence) classify sources down to a flux of 5×10^{-14} ergs cm^{-2} s^{-1} in the 0.5–10 keV energy range. Sources with high absorption ($N_H > 10^{22}$ cm^{-2}) are not properly classified indicating that detecting soft energy photons < 2 keV is crucial to distinguish between Poisson noise and emission lines. The degrading soft energy response of *Chandra* ACIS makes it difficult to combine observations from different epochs and reduces the number of soft energy X-ray photons detected, thus negatively affecting the classification accuracy.

AXIS can provide significant improvements in this area due to its larger effective area and field of view, reduced detector background, and better soft energy response. We use the distribution of COUP and CDFS parameters with AXIS FOV-average effective area, response-matrix files, and non-X-ray background, and 100ks exposure to simulate X-ray spectra of stars and AGN with AXIS and test the improvements in classification accuracy. Our results show that we can classify active stars and AGN with an accuracy of $> 90\%$ throughout our range of absorbed flux i.e $> 2 \times 10^{-15}$ ergs cm^{-2} s^{-1}. In terms of net counts, we still need > 200 net counts and $N_H < 10^{22}$ for classifying with an accuracy of 90%. If we assume that

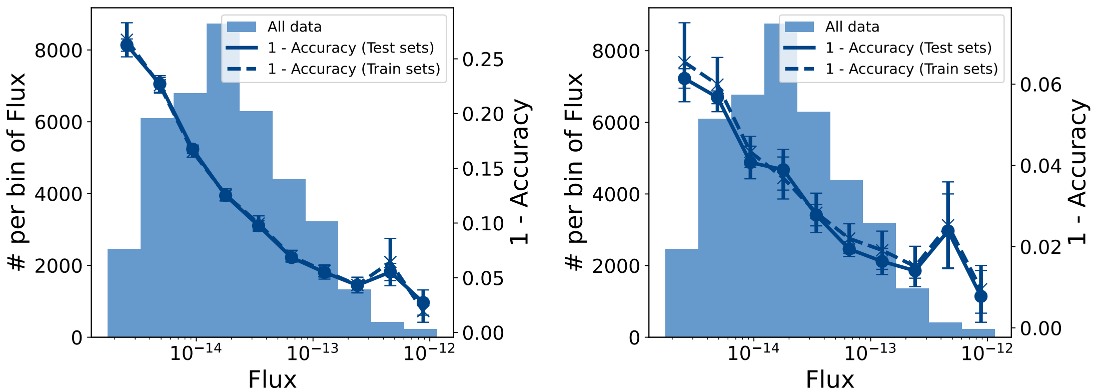

Figure 6. Comparison of ML classification on *Chandra*, *(Left)* and AXIS (*Right* spectra with exposure of 100 ks using a 1-layer, 10-node ANN. The X-axis shows the absorbed flux in the 0.3–8.0 keV energy range. The left y-axis shows the number of simulated spectra in each bin of the histogram, and right y-axis shows the error in classification with flux. The dashed lines show the error in the training dataset used for fitting the ANN, and the solid line shows the error in applying the trained ANN to an independent test set. We see that with AXIS we can accurately classify >90% of sources throughout our range of fluxes used for simulation. Note that we still require $N_H < 10^{22}$ cm^{-2} and > 200 net counts for identifying line-dominated star spectra, but the larger effective area and better soft energy response allows us to probe fainter sources.

the AXIS effective area is 10x times that of Chandra and assume a similar exposure map of *Chandra* and AXIS, we can estimate that sources with $>= 20$ net counts in the *Chandra* ACIS 0.5-7 keV can be classified accurately. The *Chandra* Source Catalog 2.0 has $\sim 2.1 \times 10^5$ such sources. Among these sources, 1.7×10^5 sources have Galactic $N_H < 10^{22}$ cm^{-2}. In comparison, 3.4×10^4 sources have net counts > 100 (2.5×10^4 of these source also have Galactic $N_H < 10^{22}$ cm^{-2}). Therefore, incorporating AXIS's 9 times larger field of view, we can anticipate that AXIS should be able to classify of order of 35 to 60 times more X-ray sources than can be classified using Chandra data.

2.2.2. Millisecond pulsar population in Galactic Bulge

The Fermi-LAT observations of the Galactic center show an excess in the γ-ray emission (Galactic Center Excess, [GCE]) in addition to that from known point sources and the Galactic ridge. While some studies have shown that this excess radiation is consistent with annihilating dark matter [e.g., 70,134], others have suggested that the GCE could be explained in its entirety through a population of unresolved millisecond pulsars (MSPs) [e.g., 1,96]. As MSPs also emit X-rays, we will be able to detect individual MSPs through X-ray telescopes having much better angular resolution than Fermi (*Chandra* has an aimpoint resolution of 0.5", and XMM-Newton has a resolution of 10"). Thus understanding the population of the MSPs in the Galactic Center and Bulge will allow us to put further constraints on the origin of the GCE. However, the soft energy X-rays (below 2 keV) from most MSPs in the Galactic center and bulge are absorbed by the high interstellar extinction towards that region. Only bright MSPs with hard spectra (through magnetospheric X-ray emission or from inter-binary shock in redback MSPs) can be detected by X-ray telescopes. If all of the GCE is from an MSP population with properties similar to that of globular clusters, we will be able to detect $1 - 86$ MSPs with $L_{X,0.3-8keV} > 10^{33}$ ergs s^{-1} or $20 - 910$ MSPs with $L_{X,0.3-8keV} > 10^{32}$ ergs s^{-1} in the Galactic Bulge [333].

Hard X-ray emission from intermediate polars (IPs) and background AGN can cause confusion in the type of source detected. Spectroscopic analysis or identifying Fe lines might be crucial to distinguish MSPs and IPs. XMM observations of the Galactic bulge suffer from a large amount of diffuse emission in the

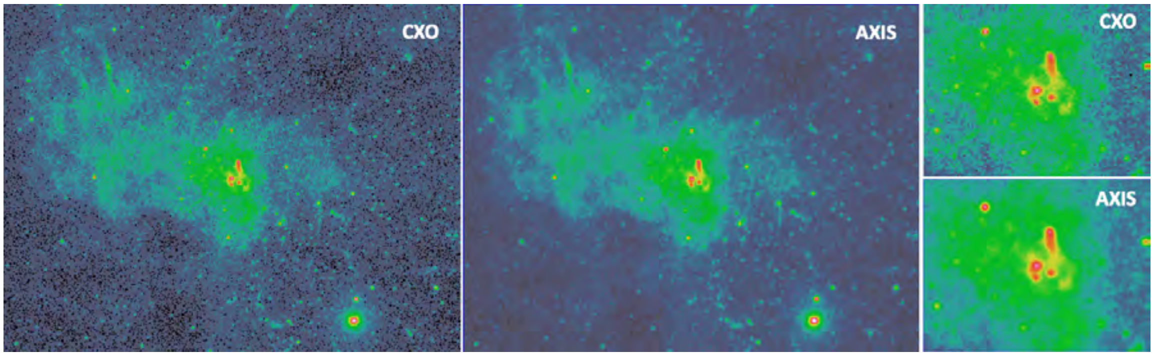

Figure 7. *Left:* 1 Ms of *Chandra*/ACIS-I imaging of the GC obtained during its first 10 years in orbit ($\sim 2.0' \times 1.45'$). *Right:* Simulated *AXIS* image of the same region as depicted on the left. The summed exposure time is 102 ks, consisting of 34 $\times$ 3 ks exposures randomly dithered within a $1' \times 1'$ box centered on Sgr A*. The subsequent stack is combined using drizzle methodology and enables statistically significant detection of all sources in the ACIS-I image. The cutouts on the right show zoom-ins on Sgr A* ($\sim 27'' \times 20''$).

region and we can only distinguish whether Fe lines are present or not in point sources with luminosities down to $L_{X,0.3-8keV} = 2 \times 10^{33}$ ergs s^{-1}. While *Chandra* has a smaller PSF, and thus less contribution from the diffuse emission, we will need deeper observations and several pointings to scan the entire Galactic Bulge. The larger effective area, wider field of view, and high angular resolution of AXIS will be able to study these sources with fewer pointings and reduced background contribution with a smaller exposure time.

3. Galactic Center and Sgr A*

The Milky Way is an archetypal disk galaxy, lying near the peak of the galaxy mass function. The Milky Way contains a SMBH at its center that lies on the M_{BH}–σ relation. At a distance of 8 kpc ($1'' \sim 0.04$ pc), our Galactic nucleus presents the observational test-bed in which to understand the extremes of star formation and black hole growth in our home galaxy. Deep spatially uniform imaging spectroscopy of the Galactic center will place direct constraints on feedback processes in an average disk galaxy as the outflows (kinetic/radiative) from Sgr A* and the vigorous star-formation taking place in the Galactic center interact with the immediate environment, the nuclear star cluster, nuclear stellar disk and the reservoir of molecular gas in the CMZ. This program of observations will inform modeling efforts to understand the physical processes driving the observed connection between galactic bulges and their super massive black holes. All of this science requires a next generation high spatial resolution X-ray observatory – *AXIS*. An example of the expected performance of *AXIS* for Galactic center science is displayed in Fig. **??**.

Sgr A* is the supermassive mass black hole at the center of the Milky Way, $M_{BH} = (4.07 \pm 0.1) \times 10^6\ M_{\odot}$, $d_{GC} = 8.1 \pm 0.1$ kpc [92,199]. Pioneering observations with *Chandra* have revealed X-ray emission from the accreting black hole, as well as emission from the broader Bondi-flow feeding the black hole [18,19,313]. Sgr A* is a low luminosity black hole with an Eddington scaled accretion rate $L_x/L_{Edd} \sim 10^{-9}$ erg s^{-1}($L_x \sim 10^{33}$ erg s^{-1}, 2-10 keV). Studies of our black hole thus provide insight into the canonical accretion mode of supermassive black holes in the Universe.

3.1. Sgr A* Flares

Sgr A* is known to have a moderate $\sim$ 10x flare at X-ray energies on a daily basis [209,210]. These flares are accompanied by counterparts in the nIR and sub-mm/radio [73,74]. Current campaigns have presented tentative evidence for the nature of the flaring mechanism; however, the difficulty of planning large multi-wavelength campaigns places limits on the observing opportunities given the known flaring rate of Sgr A* [209,210]. *AXIS* will provide advances in 2 primary ways, (i) the increased sensitivity will open up a population of more common lower luminosity flares to detailed study and, (ii) the scheduling flexibility of the observatory will aid the planning of the required large multi-facility campaigns.

The study of flaring from Sgr A* demands a multi-wavelength approach and observations across the electromagnetic spectrum are required to extract constraints on the physical mechanism responsible for the flaring, e.g., [34,35,79,317]. The mechanism driving the variability observed across the EM spectrum has not been identified, with a number of competing models proposed, ranging from magnetic re-connection or instabilities in the accretion flow, to jetted ejection events and expanding plasma "blobs" [68,71,72,75,174,186,326,329].

The Sgr A* flare X-ray flux distribution has been constrained by *Chandra*. The quiescent emission is consistent with a steady Poisson process component ($f_x \sim 4.5 \times 10^{-13}$ erg s^{-1} cm^2, 2 – 8 keV) in addition to flaring which can be described with a powerlaw ($\xi \sim 1.9$). When characterized as a log-normal process, the median flare flux is $\sim 4 \times 10^{-14}$ erg s^{-1} cm^2 (2 – 8 keV), with the flaring component contributing 10% – 15% of the quiescent flux [209,210]. *AXIS* observations will revolutionize the study of Sgr A* flaring activity, facilitating constraints on the X-ray spectra and morphology for flares deep into the known flare luminosity function. The most luminous flares (1000x) are rare but provide some of the best constraints on the broadband emission mechanism [110,216,237]. *AXIS'* observing modes will enable high time resolution spectroscopy during these events that will compliment the advanced capabilities of multi-wavelength facilities in the 2030s.

The *Gravity* and *EHT* projects have provided pioneering advancements in our capability to study Sgr A* in recent years [77,78,99,100,288]. These projects have plans to enhance their capabilities for the 2030s [101,142]. A sensitive high spatial resolution X-ray observatory is required. *AXIS'* combination of scheduling flexibility, flux sensitivity and spatial resolution will ensure access to the physics of these flares at X-ray energies. These X-ray observations will complement coordinated multi-wavelength observations from facilities such as *ELT/Roman/Gravity+/ngEHT* promising a revolution in our understanding of the accretion flow, relativistic spacetime, and the SMBH at the center of our galaxy.

An opportunity of particular interest will present itself in 2034 when S2 will make its next periastron passage $\sim$ 120 AU ($\sim$ 2800 R_{Schw}) from Sgr A*. Observations in the years surrounding the 2018 periastron passage have presented evidence for a changing flaring rate temporally associated with this event and the periastron passage of the G2 object [13,200,236]. Coordinated observations across the EM spectrum are required to constrain the flaring mechanism, and the flexible high spatial resolution X-ray observations provided by *AXIS* will be the only way to constrain the X-ray emission during these campaigns in the 2030s.

3.2. The Quiescent Accretion Flow & Bondi Flow

The quiescent emission from Sgr A* is consistent with thermal bremsstrahlung in the X-ray band, emitted by an outflow-dominated accretion flow within the BH Bondi radius [313]. Observations with *AXIS* will open up the possibility of new time domain studies of this quiescent accretion flow. *Chandra* observations have demonstrated the flow to be outflow dominated. *AXIS* observations will probe the variation of this plasma for the first time and constrain the variation of the continuum with respect to variations in the Fe XXV emission line revealed by *Chandra*.

Of particular interest are the interactions of the S-stars with the hot gas, e.g., S2 approaches $\sim$ 120 AU ($\sim$ 17 light-hr) from Sgr A* during periastron passages [99]. The next passage will occur in 2034 and observations of the quiescent flow and its response to the S2 star passage will be illuminating. There are

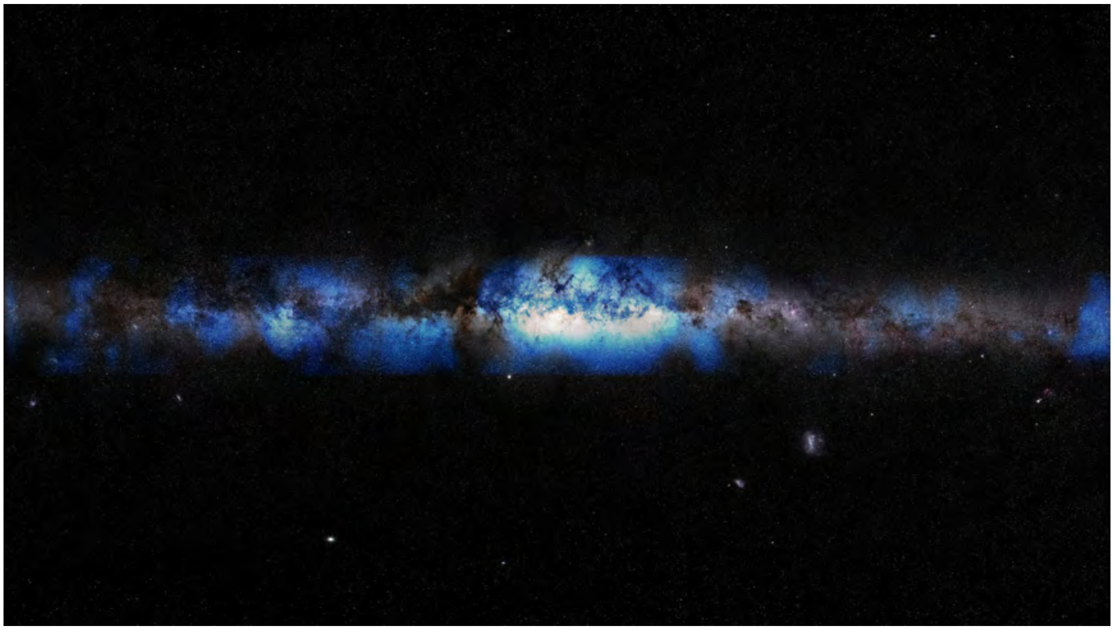

Figure 8. An artist's composition of the Milky Way seen with a neutrino lens (blue). Credit: IceCube Collaboration/U.S. National Science Foundation (Lily Le & Shawn Johnson)/ESO (S. Brunier)
there is this icecube plot, and the multiwav panel plot... though that doesn't contain X-rays and would require we do some editing// perhaps adding the survey boxes from fig 1. on this would work??

also an emerging population of so-called G-objects in the vicinity of the Sgr A* in addition to a recently identified filamentary feature that may be breaking up as it approaches the SMBH, e.g., [53].

AXIS' sensitivity will enable studies of the spatial morphology of the diffuse emission associated with the accretion flow in addition to placing constraints on the radial temperature distribution of the plasma. Winds from massive stars in the central 2 pc have been shown to be capable of fueling the SMBH [38,60,61,251,251,274], and these winds in turn can interact with and disrupt the circumnuclear disk, driving further gas towards the black hole [251]. Of key interest will be going below the sensitivity limit of *Chandra* to study the extended diffuse emission in the outer accretion flow and place observational constraints on hot plasma in the transition region where the stellar winds from stars in the circumnuclear disk feeding the SMBH slow and enter the black hole's sphere of influence [60,61,274]. Potential variable jetted emission from Sgr A* may also impact the inflowing gas [251,330,337].

3.3. Stellar Populations in the Galactic Center

Stellar evolution predicts a large population of stellar mass BHs and neutron stars in the Galaxy. In the Galactic center, dynamical friction should result in the accumulation of a large number of stellar mass BHs in the vicinity of Sgr A* [83,188,193,198]. Many X-ray sources have been detected in the GC by *Chandra* [133,201,203,206,336] and a fraction of these have been interpreted to display the characteristics of a population of quiescent stellar mass black holes [112,197]. The nature of these sources is contentious [179,195] and high spatial resolution X-ray observations are required to enable further progress on this question.

AXIS observations will also facilitate observations of massive star forming clusters (e.g., Arches, Quintuplet, IRS 13E), those in the process of forming (e.g., Sgr B2), in addition to X-ray sources in the nuclear star cluster and nuclear stellar disk [39,84,87,93,310,312].

3.4. Diffuse X-ray Emission

AXIS will carry out a deep uniform survey of the Galactic center. The combination of excellent sensitivity in the 2–10 keV bandpass and a uniform PSF across the FoV will enable the detection of the hot plasma content extending from Sgr A* to the circumnuclear ring ($\sim$2 pc, $\sim 50''$) and out to the CMZ (r $\sim$200 pc, $\sim 80'$) and beyond. Spatially uniform *AXIS* imaging across the Galactic center will reveal the X-ray emission morphology in this entire region at arcsecond resolution ($\sim$0.04 pc at 8 kpc), and enable constraints to be placed on the physical state of the hot plasma and the source populations/processes which generate it, e.g., [12,170,203,215,294].

A key *AXIS* goal will be searching for connections linking the abundant plasma filling the GC and the *Fermi* bubbles [285] (with prominent counterparts observed at X-ray and radio wavelengths [42,246]). Observations on smaller spatial scales have demonstrated the existence of the 'so-called' GC chimneys, which reveal 100-pc scale X-ray outflows from the GC region towards the *Fermi* bubbles [207,239]. The observation of molecular gas counterparts demonstrates the multi-phase nature of this outflow, and presents a prime example of ongoing in-situ feedback [234,305]. In the immediate vicinity of Sgr A*, X-ray emission suggesting the presence of jets originating from the black hole will be constrained [330,337].

Large scale mapping of the GC at radio wavelengths has revealed diverse extended structures (see Fig. 2, [126]). The thin filamentary structures detected therein, unique to the GC, are of particular interest and are thought to be a result of the intense SNe and SMBH feedback in the GC [273,328]. Molecular clouds near Sgr A* have been shown to exhibit strong and variable X-ray fluorescence [160,235]. *AXIS* observations will constrain the location and morphology of the Fe K-shell emitting gas on unprecedented spatial scales, enabling study of the spatial distribution and structure of dense molecular gas in the Galactic center [51]. Comparison of Fe-K maps on multi-year timescales will enable a sensitive study of its variation across the molecular clouds with time. These observations will facilitate the creation of a high time resolution record of the past activity of Sgr A* [40,50,55,185] and provide constraints on the cosmic ray population [256] in the Galactic center.

The proposed *AXIS* studies of the GC region will have a clear multi-messenger component given the *IceCube* detection of a neutrino flux consistent with an origin in the Galactic plane ([137], see Fig. **??**). Searches for a discrete point-like (e.g., XRBs, pulsars, Sgr A*) or extended (e.g., SNRs) source population of Galactic neutrino emitters has thus far returned null-results, although a number of candidate sources are present at $< 3\sigma$ level [2,3]. As the S/N continues to build in coming years we can expect a catalogue of Galactic neutrino sources to emerge. This discovery opens a new path to study the Milky Way and the high spatial resolution and sensitivity of *AXIS* will play a key role in our exploration of the sites of galactic cosmic-ray generation and the multi-messenger Milky Way in the next decade.

4. Clusters (Open and Globular)

Open clusters are the primary birthplaces of compact objects (COs; referring here to neutron stars and black holes) in the galaxy, but given that for most of them, their total masses are relatively low ($\lesssim 1000\ M_\odot$ [228,229]) and not centrally concentrated (i.e., as in globular clusters), a majority of COs quickly escape their birth clusters (see e.g., [192,265,300]). However, COs formed in very massive ($M_\odot > 10^4$) and young ($\lesssim$ 10 Myr) stellar clusters may still reside in them. In this respect, the Chandra discovery of a young magnetar in the outskirts of the $\sim$ 5-Myr-old Westerlund 1 open cluster is encouraging [204]. However, if other, less luminous COs (e.g., older magnetars, NSs, or BHs with a low level of accretion), exist in these clusters, they would be difficult to find/identify with the existing X-ray observatories. Discovering such objects in their natal environments allows one to place very tight constraints on the properties of the progenitor star and SN explosion models [204]. AXIS will enable the discovery of new COs in open clusters given its high angular-resolution (necessary to resolve the many point sources in crowded environments

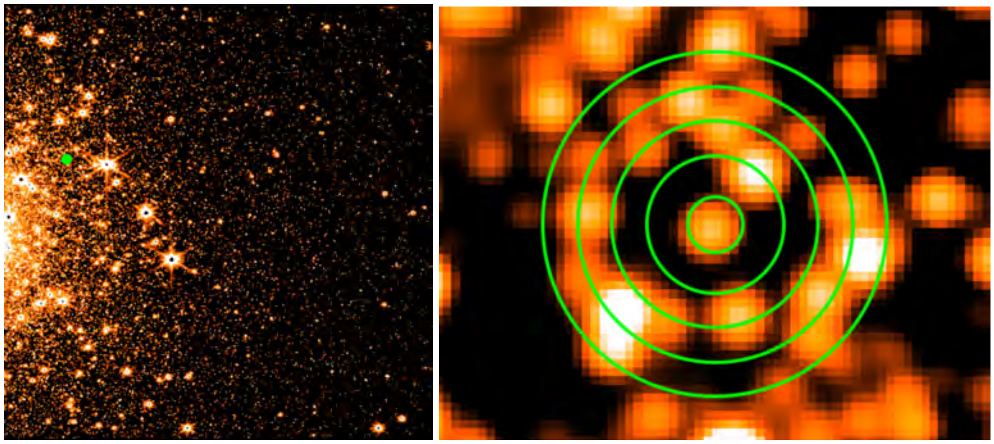

Figure 9. *Left:* JWST NIRcam F277W image of the Galactic globular cluster M92. The green point shows the location of the zoom in on the right panel, note that it is outside of the core of the cluster. *Right:* Zoom-in showing hypothetical positional error circles of an X-ray source outside of the cluster core. The circles have radii of 1.25", 1", 0.75", 0.5", and 0.2", respectively. Note that the number of potential IR counterparts detected by JWST drops dramatically with increasing X-ray positional accuracy, afforded by AXIS's exceptional PSF, allowing for confident identifications of optical/IR counterparts to X-ray sources.

and to provide accurate source positions), high sensitivity, and large field of view. As open clusters age, the most massive of them remain bound, retaining a fraction of their stars. It's possible that these older clusters can retain COs, if a fraction of the COs experience small kicks and/or are born in binaries. For example, neutron stars born from electron-capture supernovae are thought to receive low enough kicks to be still bound to their birth clusters [94,138,280]. Chandra studies of these clusters, with varying ages, have uncovered a plethora of different source types, but a CO has yet to be found, with the exception of the magnetar in Westerlund 1 (see e.g., [48,95,297,304]).

Globular clusters (GCs) host an overabundance of accreting COs per unit mass when compared to the Galactic disk. This is due to the large number of dynamical interactions occurring in the dense cores of these clusters, which leads to an increased number of tight binaries [54]. High angular resolution X-ray observatories are needed to study the X-ray source populations in GCs due to extreme source crowding in the cluster cores. Chandra has played a pivotal role in advancing our understanding of X-ray source populations in GCs, particularly at the fainter luminosity end (see e.g., [109,120–122,124,241]). A number of interesting source classes hosting COs are typically found at these fainter luminosities (i.e., $L_X \lesssim 10^{32}$ erg s^{-1}), including quiescent low-mass X-ray binaries with NSs (qLMXBs) [123], MSPs (see e.g.,[28,29,334]), and an emerging population of candidate BH LMXBs [20,49,191,281], one of which recently underwent an outburst and produced radio jets [22,227]. Discovering more of these systems allows for understanding the dynamical production and destruction of binaries, as a function of encounter rate, metallicity, cluster structure, and other properties (see e.g., [240,242]). AXIS will enable deep and efficient surveys of a majority of the Galactic GCs down to luminosities of $L_X < 10^{30}$ erg s^{-1}. Pushing to lower luminosities in a large number of GCs is critical for identifying new unique objects, such as BH LMXBs, several of which have quiescent luminosities $L_X < 10^{30}$ erg s^{-1} [118,281]. By identifying more of these systems (in concert with deep radio studies), we can start to understand their formation rate in comparison to the binaries hosting NSs. This has important implications for the rate of BH-BH mergers being detected by LIGO (see e.g., [14,15,332]).

GC science is also inherently a multiwavelength science. AXIS will be able to leverage the rich pre-existing multiwavelength data sets from radio to GeV wavelengths, as well as new observations from,

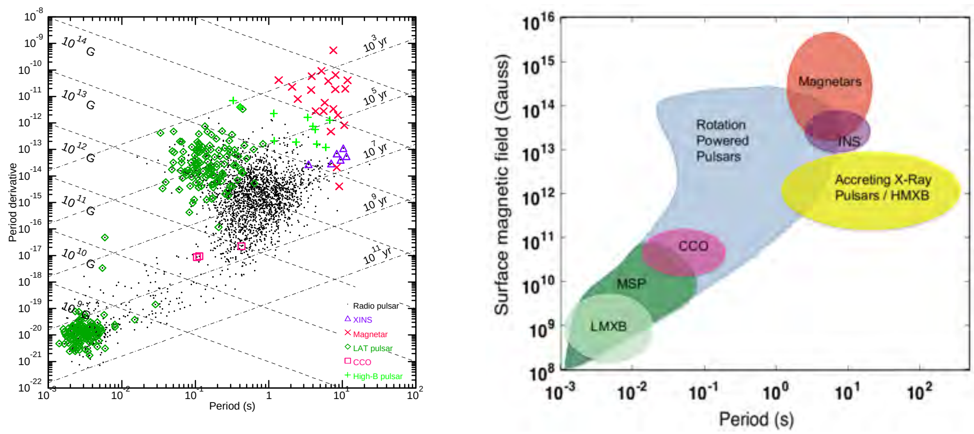

Figure 10. The P-$\dot{P}$ diagram constructed using pulsars in the ATNF catalog (left) and a schematic diagram of P *vs* B_s taken from Harding [114].

for example, JWST. Optical and IR data from HST, JWST, VLT/MUSE, Gemini/GIRMOS, and Gaia can be used to place tight constraints on the distance, age, mass, and metallicity of GCs, and to search for the optical/IR counterparts of the X-ray emitting sources (see Figure 9 and e.g., [116,121,263]). Having very accurate distance measurements allows for more accurate estimates of NS masses and radii (see e.g., [30,44,105]), which are necessary for constraining the NS equation of state. Additionally, the physics of the crust of NSs can be probed by observing how they cool after undergoing an accretion episode (see [65,219,316]). Another example is the MSP population of GCs, which is typically uncovered by radio observatories and then can be followed up in X-rays (see e.g., Terzan 5 [28,248]). In particular, X-ray observations have shown that this population is diverse ranging from isolated MSPs to tight spider binaries. These systems are composed of redback binaries, where the MSP wind interacts with the low-mass companion, and the even more extreme black-widow binaries, where the pulsar wind completely ablates the companion star (see e.g., [282,287]). A repeating fast radio burst (FRBs) has also recently been discovered in an extragalactic GC [164], suggesting GCs host some fraction of repeating FRBs. Sensitive X-ray observations of Galactic GCs will help to test FRB models and what types of sources are capable of producing them. As new observatories come online over the next decade (e.g., SKA, CTA, Roman) and discover new COs, the lack of a next generation sensitive, high angular resolution X-ray observatory to replace Chandra, would greatly hinder Galactic GC science (see Figure 9). AXIS will enable the continuation of this science and inevitably lead to many new discoveries that will help to further our understanding of COs and GCs.

5. Compact Objects: Isolated Neutron Stars

A neutron star is the left-over core of a massive star that underwent a supernova explosion. When the progenitor is massive enough, the star may collapse to compress the core to the density at which neutron degeneracy pressure kicks in and keeps the star from further collapse. The density of the core at this point is above nuclear density, and the core has a radius of $\sim$10 km and a mass of $\sim 1.4 M_{\odot}$. A neutron star can have a rapid spin and strong magnetic field (B), e.g., if the angular momentum and magnetic flux of the progenitor were conserved during its collapse. Neutron stars provide a unique laboratory to probe the most dense matter and the highest B in the Universe, giving opportunities to revolutionize our understanding of physics in extreme environments [see 114,154,258, for reviews].

5.1. Population of Isolated Neutron Stars

Neutron stars are generally discovered as pulsating (rotating) sources in the radio, X-ray, and gamma-ray band; these pulsating neutron stars are called pulsars. Radio, X-ray, and gamma-ray observatories have served as excellent tools in studying neutron stars for decades, and they helped clarify observational properties of neutron stars. At the same time, discoveries of more neutron stars have complicated the simple and fundamental picture for neutron stars, dense matter under strong B, as is displayed in the diagrams (Figure 10) of the spin period (P) *vs* its time derivative ($\dot{P}$), and P *vs* the spin-inferred surface magnetic field strength ($B_s = 3.2 \times 10^{19}\sqrt{P\dot{P}}$). Neutron stars have been categorized into several classes: rotation-powered pulsars (RPPs), X-ray dim isolated neutron stars (XDINSs), central compact objects (CCOs), millisecond pulsars (MSPs) and magnetars based on their grouping in the P-$\dot{P}$ diagram and emission properties. It was suggested that these neutron-star classes are all linked to one another via magnetothermal evolution [e.g., 225,244,306], which may help unify the diverse classes into one, allowing us to understand the state of the most dense matter under extreme B. We describe basic observational properties of the neutron-star classes in relation to the AXIS observatory, and discuss how it can help understand neutron stars better. Here we focus on 'isolated' neutron stars (i.e., not in a binary) and their observational properties.

RPPs are neutron stars whose electromagnetic emission is powered by rotational energy of the pulsar (spin-down power $\dot{E}_{\rm SD}$). They are mostly detected in the radio band, but some of them are detected in the X-ray and gamma-ray bands. X-ray emission from many RPPs is dominated by nonthermal emission, both magnetospheric and from surrounding PWNe. AXIS can help distinguish these, via spatial resolution for many PWNe and, for young pulsars, by gating out pulsed magnetospheric flux. Many RPP sources emit thermal blackbody (BB) emission as well [e.g., 244,335] and some RPPs show only thermal emission. These thermal emissions are particularly important since they can provide important clues to the evolution of neutron stars and fundamental physics; e.g., the low thermal luminosity ($L_{\rm BB}$) of the young PSR J0205+6449 in 3C 58 [272] has been interpreted as due to rapid cooling via the direct URCA process enabled by high proton fractions in the core of neutron stars with mass $\geq 1.6 M_\odot$ for certain nuclear equations of state [244].

XDINSs are neutron stars which do not have an associated supernova remnant, a binary companion, or a pulsating radio counterpart. Until now, twelve sources, including candidates, were discovered, and their emission is primarily in the X-ray band. Spectra of XDINSs are well characterized by $kT =$ 0.045–0.1 keV BB emission with broad absorption features (and some UV and X-ray excess). XDINSs have $P = 3 - 17$ s and $B_s \sim 10^{13}$ G which overlap with magnetars in the P-$\dot{P}$ diagram (Figure 10). Large $L_{\rm BB}/\dot{E}_{\rm SD}$ values estimated for XDINSs, sometimes exceeding 1 [1RX J0720.4−3125; 147], may imply that their high B plays an important role in their emission like in the case of magnetars. Hence it has been suggested that XDINSs are descendants of magnetars [141] since the former have very similar spin and emission properties to the latter but much larger characteristic age τ_c of typically $\geq 10^6$ yrs.

CCOs are young and radio-quiet isolated neutron stars discovered near the center of SNRs. Spectra of CCOs are well characterized by thermal blackbody-like emission with X-ray luminosity of $\sim 10^{33}$ erg s^{-1}, and one source has strong harmonically-spaced absorption lines [see 63, for a review]. While these emission properties are very similar to those of XDINSs, CCOs have very different spin properties from XDINSs [but see properties of the XDINS 1RXS J141256.0+792204 (Calvera); 31,331]. Pulsations of CCOs with $P \approx 100 - 400$ ms were detected in three sources [97], and their spin-inferred B_s and τ_c are $3 \times 10^{10} - 10^{11}$ G and $> 10^8$ yr, respectively (Figure 10). Note that their τ_c values are orders of magnitude larger than the estimated ages of the host SNR. In an evolutionary model [127], it was suggested that CCOs have high B which were initially submerged. The re-emerging B results in an increase of $\dot{P}$, and the CCOs will eventually evolve to join the RPP population.

Magnetars[1] are young neutron stars with ultra-strong B well above the quantum critical field of 4.4×10^{13} G. They are slow rotators with P=2–12 s and emit strongly in the X-ray band [see 155,187, for reviews]. Their quiescent luminosities often exceed $\dot{E}_{\rm SD}$, and thus it was theorized that the emission is powered by the decay of the enormous B [289]. Spectra of magnetars are well described by thermal BB from the hot surface and nonthermal radiation from the magnetosphere. The nonthermal emission is described by a soft power law $<$10 keV but a dramatic spectral turn-over at $>$10 keV has been seen in many magnetars [e.g., 172]. The hallmark characteristics of magnetars are $<$1 s bursts and months-long outbursts during which their X-ray and/or soft gamma-ray emission increases by orders of magnitude [e.g., 156]. Because these emission properties (e.g., $>$10 keV spectral turn-over and outbursts) are very different from the other classes of neutron stars, it was thought that magnetars form a distinct class. However, magnetar-like outbursts from the typical high-B RPPs PSR J1846−0258 [89] and PSR J1119−6127 [325], and discoveries of low-B magnetars [e.g., 8,250,262] blurred the distinction significantly. These suggest that magnetars are neutron stars in a different stage of their magnetothermal evolution [e.g., 244,306].

5.2. Important questions on Isolated Neutron Stars which AXIS can help address

Although various X-ray observatories such as Chandra, XMM, Swift, and NuSTAR have helped understand neutron stars in great detail during the previous two decades, a lot of important questions on neutron stars still remain unanswered. We list a few of them below.

1. Relation between the diverse classes of neutron stars: It was suggested that neutron stars born with different birth properties (e.g., B) evolve along different paths and exhibit diverse observational properties; e.g., it was suggested that magnetars evolve to become XDINSs [e.g., 141], and CCOs become RPPs [127]. The evolution effects may be observed as correlations between the emission and spin-inferred properties. Correlation studies have been performed with neutron stars in different classes [e.g., 10,128,194,231,335], which found correlations between kT and B_s and between $L_{\rm BB}$ and B_s in neutron-star samples taken from multiple classes, thermally emitting RPPs, XDINSs, and magnetars. These findings suggest that neutron stars have the same power sources [e.g., residual heat and decay of B; 231] but their relative contribution differs from class to class, providing important clues toward unification of neutron-star models. However, the sample sizes used in these studies were small, and the correlation significance was not very high. Moreover, relations between the properties (e.g., inferred from power-law fits) could not be measured precisely. These can be substantially improved by increasing the sample size of thermally-emitting neutron stars. AXIS with its large effective area and high angular resolution across the field of view (FoV) will discover more highly-absorbed (i.e., at large distances) low-kT neutron stars (e.g., high-B RPPs, XDINSs, CCOs, and transient magnetars in quiescence) that have not been detected by current X-ray observatories.
2. Long-term evolution of neutron stars over time scales of $>$ Myr: Magnetothermal evolution models [225,244,306] have shown that long-term evolution of neutron stars depends on their physical properties such as internal B, core temperature, and the state of the dense matter. Note, however, that the samples used in these studies might be biased to high-$L_{\rm BB}$ sources because low-$L_{\rm BB}$ ones are difficult to discover. Nonetheless, in these models neutron stars in the diverse classes differ only in their birth properties and their evolution; these generate the observational diversities. The "neutron-star unification" schemes seem to successfully explain the $L_{\rm BB}$ *vs* age trend [e.g., 244,306] and the magnetar-like outbursts from typical (high-B) RPPs [PSR J1846−0258 and PSR J1119−6127; 89,325] as due to magnetothermal evolution effects [225,306]. The authors predicted that outbursts of

[1] https://www.physics.mcgill.ca/∼pulsar/magnetar/main.html

older and low-B (e.g., compared to magnetars) pulsars would be less frequent and have less energy. Then, two outbursts from the typical RPP PSR J1846−0258 on a time scale of $\sim$10 yr, which seems as frequent as ones in magnetars with much higher-B, are very challenging to explain. This may indicate the true B of a neutron star is different from the spin-inferred B_s [e.g., hidden toroidal component; 225], but only three magnetar-like outbursts were detected from two RPPs. So the unification models need to be scrutinized with larger samples of magnetar-like outbursts and low-$L_{\rm BB}$ RPPs. Particularly useful for the study of the long-term evolution is a very young neutron star whose cooling can be detected on a time scale of order 10 years. Ho et al. [129] and Shternin et al. [267] suggested, using Chandra data spanning $\sim$19 yr, that the surface temperature of the $\sim$350-yr-old (inferred from the SNR expansion) CCO CXOU J232327.9+584842 in the Cas A SNR decreased at a 10-year rate of 2–3%. If so, the CCO provides a unique opportunity to probe initial cooling of newly-born neutron stars and fundamental physics, such as the presence of a neutron superfluid and proton superconductor in the star [220,267,268]. While the results of Ho et al. [129] were reproduced by Posselt & Pavlov [243], the latter noted that the changes of the fit-inferred temperature can alternatively be explained as due to systematic effects caused by, e.g., extra contamination of the ACIS filter beyond that accounted for in existing calibration information [230]. This controversy can be resolved by AXIS observations, which may also be able to measure potential temperature declines in other (slightly older) CCOs Ho et al. [see e.g. 129].

3. Short-term flux relaxation over time scales of years after magnetar outbursts: Magnetar outbursts can also tell us much about physics under extreme conditions; magnetar outbursts were suggested to be caused by crustal deformation and/or twist of the external B [289]. Mechanisms of the outbursts and their relaxations are not yet well understood, but it is thought that the change of the thermal emission is related to crustal cooling [e.g., 168] whereas the change of the nonthermal emission is influenced by magnetospheric relaxation [26]. In the case of crustal cooling, the declining trends of $L_{\rm BB}$ with time after outbursts can provide important insights into the dense matter in the crust [e.g., location of the energy deposition and core temperature; 9]. In particular, the late-time cooling trend (on time scales of thousands of days) is sensitive to the properties of the deep inner crust [e.g., nuclear-pasta phase; 135,233] and can help probe the state of the dense matter near the core [e.g., 66]. For such studies, observations of outburst relaxations of faint magnetars are desirable because for bright magnetars amplitudes of the relative flux enhancement and subsequent relaxation, significantly affected by neutrino emission [e.g., 232], are very small. As transient magnetars in quiescence may be very faint having a 0.5–10 keV flux of $< 10^{-14}$ erg s^{-1} cm^{-2}, current X-ray observatories have not followed the cooling trends down to very low-flux levels. AXIS will allow accurate characterizations of the late-time cooling trends of faint and transient sources and make it possible to probe properties of deep inner crusts of magnetars.

5.3. AXIS simulations for Isolated Neutron Stars

As noted above (Section 5.2), AXIS can make significant contributions to our understanding of isolated neutron stars by characterizing thermal emission of faint sources and by discovering more (and exotic) sources. Accurate characterizations of RPPs are crucial not only to population studies (e.g., correlation and cooling) but also to measurements of their PWN emissions since the pulsars' nonthermal emission can contaminate the PWN emissions in low-spatial-resolution observations. Some RPPs (including high-B RPPs) are observed to have only faint BB emission, and it was difficult to measure their kT and $L_{\rm BB}$ for population studies [e.g., 244,335]. The left panel of Figure 11 shows as an example a spectrum simulated for an AXIS observation of a faint high-B RPP [PSR J1734−3333 with the 0.5–2 keV flux of 3.6×10^{-14} erg s^{-1} cm^{-2}; 217] whose spectral parameters were not well constrained by a 125 ks XMM observation even with frozen $N_{\rm H}$. A 10-ks AXIS observation can constrain the flux and kT to within 6%

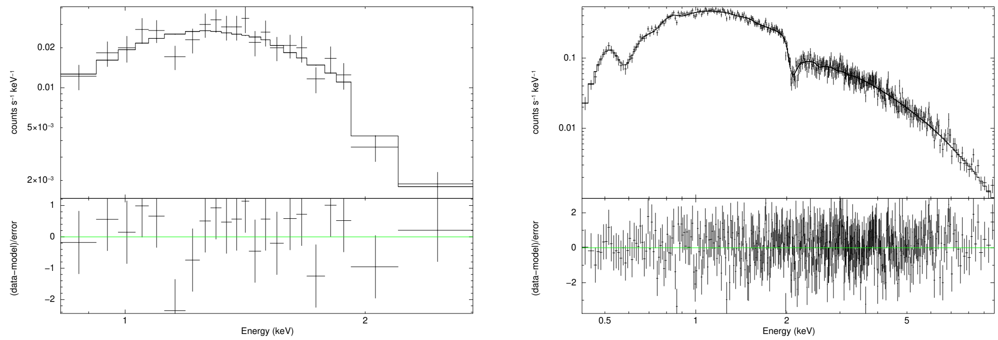

Figure 11. Spectra of the RPPs PSR J1734−3333 (left) and PSR J0205+6449 (right) simulated for a 20 ks and 50 ks AXIS observation, respectively. For PSR J1734−3333, we assumed a BB model having $N_{\rm H} = 6.7 \times 10^{21}$ cm^{-2}, $kT = 0.3$ keV and the unabsorbed 0.5–2 keV flux of 3.6×10^{-14} erg s^{-1} cm^{-2} [217]. For J0205+6449, we based the 50-ks simulation on a BB+PL spectrum measured by 317 ks Chandra exposure [272].

and 10%, respectively (for frozen $N_{\rm H}$), and 20-ks data can put tight constraints on the $N_{\rm H}$ (20% uncertainty) as well as the spectral parameters (30% and 10% uncertainties for the flux and kT, respectively). For some RPPs, their BB emissions are not well constrained due to contamination by the bright nonthermal emission of the pulsar and PWN. Moreover, pile-up effects in Chandra observations and large PWN+SNR background in XMM (and Chandra CC-mode) data have prohibited precise characterizations of the BB component. These can be overcome by AXIS thanks to its large effective area, and high temporal and angular resolution. BB emission has been certainly detected in some young and bright RPPs [e.g., PSR J0205+6449; 272], suggesting that there are more such sources in which the BB emission is undetected due to the strong nonthermal contamination. As 'young' RPPs with small $L_{\rm BB}$ can provide important clues to the thermal evolution of neutron stars [e.g., 244,306], discovering more young and low-$L_{\rm BB}$ RPPs is crucial to constraining the evolution models (Section 5.2). From AXIS simulations for PSR J0205+6449, we found that its faint thermal emission, which is swamped by a nonthermal power-law component (pulsar + PWN), can be detected with 3σ confidence by a 10 ks AXIS observation, and kT and $L_{\rm BB}$ can be measured to within 5% and 30% with a 50 ks observation (Figure 11). This verifies that AXIS can characterize faint BB emission of RPPs and will help scrutinize the magnetothermal evolution models.

AXIS can also increase the sample size for correlation studies. XDINSs and magnetars can be identified by AXIS as the 3–17 s pulsations can be easily detected. With a time resolution of less than 50 ms, AXIS could also measure thermal and non-thermal pulsations from RPPs with spin periods of several hundred ms; for subarray observations, even faster spinning RPPs could be detected, such as the 65 ms PSR J0205+6449. The spatial resolution of AXIS will be important to reduce non-pulsed emission from any nearby PWN and/or SNR, and the large effective area of AXIS will allow discoveries of distant and highly-absorbed sources. Figure 12 shows results of simulations for 10 ks AXIS observations of a source having $kT = 0.1$ keV and $L_{\rm BB} = 10^{33}$ erg s^{-1} (for XDINSs, CCOs, and transient magnetars in quiescence). The pulsed fraction and distance to the source were varied, and we assumed that the absorbing column density $N_{\rm H}$ increases by 10^{22} cm^{-2} per kpc. The simulations show that a 10-ks AXIS observation will be able to detect the pulsations of a neutron star at $\leq$3 kpc if its pulsed fraction is greater than 20%. Two of the currently known XDINSs (<500 pc) have a pulsed fraction of $\approx$ 20% [147], and extrapolating this to the larger space volume we anticipate AXIS will discover $\sim$70 similar XDINSs. Although this estimation is very rough, it is almost certain that the high angular resolution over the large FoV of AXIS will allow serendipitous discoveries of many XDINSs and quiescent magnetars. The latter likely having higher kT and nonthermal emission may be more easily detected.

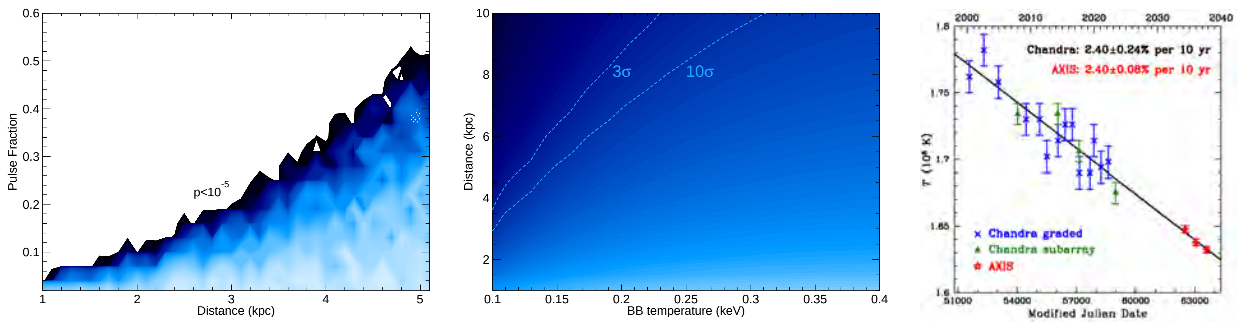

Figure 12. Simulations of AXIS observations for detections of pulsations (left) and faint sources (middle), and for measurements of the surface temperature of the CCO in the Cas A SNR. *Left and middle*: Simulations for 10-ks AXIS observations were performed for a thermally emitting (BB) source having $kT = 0.1$ keV (varying in the middle panel) and $L_{\rm BB} = 10^{33}$ erg s^{-1} with $N_{\rm H}$ increasing by 10^{22} cm^{-2} per kpc. The absorbed 0.5–10 keV flux is 2.5×10^{-14} erg s^{-1} cm^{-2} (for $kT = 0.1$ keV at 1 kpc) and decreases inversely proportional to distance squared. The white region in the left panel is where the pulsations could be detected with the chance probability less than 10^{-5}, and the contours in the middle panel denote detection significances for reference (5σ and 10σ). *Right*: We extrapolated from previous measurements of the spectra of the Cas A CCO reported by Shternin et al. [267], simulated three 50-ks AXIS spectra, and plotted the temperature inferred from the AXIS data (red points).

The 100–400 ms pulsations of CCOs might be detectable by AXIS. Identification of a newly-discovered source as a CCO can be assisted by measurements of the emission spectrum [kT=0.15–0.47 keV; 6] and the location (SNR association). We investigated how well a 10-ks AXIS observation would 'discover' a BB-emitting source within an SNR. The middle panel of Figure 12 shows detection significance for BB emission with $L_{\rm BB} = 10^{33}$ erg s^{-1} for various values of kT and distance. The results suggest that AXIS can make a 10σ detection of a CCO at $\geq$10 kpc if its kT is greater than 0.3 keV. The detection criterion (10σ instead of 3σ) we used here mitigates the influence of possible background by the PWN and SNR. The high detection sensitivity of AXIS will also allow meaningful follow-up studies of magnetar relaxation after an outburst down to a very low-flux level; e.g., a 10-ks AXIS observation could have detected the low-B magnetar SGR 0418+5729 at 2 kpc, had its flux decayed to a lower level (absorbed 0.5–10 keV flux of 6×10^{-15} erg s^{-1} cm^{-2}; 10σ detection) than the historical minimum of 2×10^{-14} erg s^{-1} cm^{-2} [250].

AXIS will be able to resolve the uncertainty of the cooling rate of the CCO CXOU J232327.9+584842 in the Cas A SNR, whose observation requires the spatial resolution of AXIS due to the diffuse X-ray bright emission around the CCO. In the right panel of Figure 12, we show current measurements of the surface temperature of the CCO and simulation results for three 50 ks AXIS observations. For the simulations, we assumed that the temperature drop is astrophysical in origin [129,267] and is not caused by systematic effects [e.g., 243]. A 50-ks AXIS observation will constrain the surface temperature to within $\sim$0.1%, and three such observations with a cadence of $\leq$2 yr are sufficient to tell whether or not the surface temperature of the source actually decreases with time. This could have significant implications on long-term magnetothermal evolution models and constraints on fundamental physics.

Thanks to its large effective area, AXIS will also allow detections and studies on spectral features from magnetars. To date, several spectral features from magnetars have been detected during quiescence as well as during bursts (see e.g. [11,88,136,249,283, line detections at various energies during bursts of several magnetars] [290, variable absorption lines throughout the rotation phase of the magnetar SGR 0418+5729]). These features are often interpreted as proton cyclotron features, as a result of photons emitted from the hotspot scattering at the cyclotron frequency in the magnetosphere. However, the extreme magnetic and gravitational fields in the region are expected to broaden such line features, making them harder to detect. Larger effective area instruments with sufficient timing and energy resolution, therefore, are crucial to be able to detect stronger spectral signatures of magnetars. Magnetar burst line detections promise insight into the exact causes of bursts and emission mechanisms. On the other hand, during quiescence, varying spectral lines in phase-resolved magnetar spectra are thought to be linked to the geometry of the magnetic field lines surrounding the emitting region [290]. More recent work shows that hotspot emission and corresponding magnetic field geometry in quiescence can be determined by constraining the exact shape of the spectral line (i.e. line width and depth) concurrently with the line energy using phase-resolved spectroscopy [163]. Overall, spectral lines also yield an estimate of the magnetar's magnetic and gravitational field as well as the size of the emitting region.

We performed simulations to check for the capabilities of AXIS in detecting spectral features of magnetars during quiescence and bursts. For quiescent emission, we focused on phase-resolved spectroscopy to test how well AXIS could detect varying spectral features throughout the rotational phase of the magnetar compared to other current/upcoming telescopes. For all simulations, we created fake spectra using the *fakeit* function on XSPEC v12.13.0 [16] with the latest public effective area and response of the respective detector. For persistent emission, we set all models and corresponding parameters to the line detections between of SGR 0418+5729 reported in [290]. For bursts, we set model parameters to the 1998 burst precursor line detection of SGR 1900+14 in [283], but scaled continuum normalization to obtain a count rate of $\sim$ 35k in 0.2 seconds duration to represent a burst-like scenario. We then fit the simulated spectra for various detectors, fixing the quiescent emission continuum model to the reported phase-averaged best-fits in [290] and SGR 1900+14 Hydrogen Column Density to the best-fit value in [283]. We freed all remaining parameters.

In Figure 13, we present the results of our simulations for magnetar spectroscopy. On the left panel, we plot the average percent errors (i.e. 1σ errors divided by the fitted parameter value) for line energy (E), line depth (D) and line width (W) for quiescent emission. Note that all values reported here are averaged over simulations for ten spectral lines detected between the phases $0-0.3$ for SGR 0418+5729 in [290]. We see that, compared to current instruments (i.e. XMM-Newton epic-pn and NICER), AXIS can detect all spectral line parameters with over a two-fold reduction in percent errors, and performs similarly to the upcoming eXTP mission. This shows that AXIS will increase our capabilities in detecting magnetar spectral lines in quiescence. Moreover, we will be able to probe hotspot emission and corresponding magnetic field geometry thanks to the capabilities of AXIS in constraining all spectral line parameters concurrently (see [163] for a more detailed description on how constraining these line features would enhance our understanding of magnetar field line geometry).

In the middle and right panels of Figure 13 we also plot the results of our simulations for magnetar bursts. Here, values reported for each detector are fitted values with corresponding 1σ upper and lower error bars averaged over 100 iterations. To test for a hypothetical spectral burst line at higher and lower energies, we re-run the simulation for a 4 keV and 8 keV line in addition to the original 6.4 keV line detection in [283], while keeping all other parameters the same. We find that overall AXIS provides the most accurate as well as precise measurements of all line parameters during the burst compared to current instruments. Since magnetar bursts tend to be extremely energetic, the large effective area of AXIS would also be useful to detect spectral lines during bursts (as opposed to several previous detections only during burst precursors likely due to pile-up limitations). Therefore, we conclude that AXIS could provide a useful tool in understanding more about magnetar bursts through spectral feature detections.

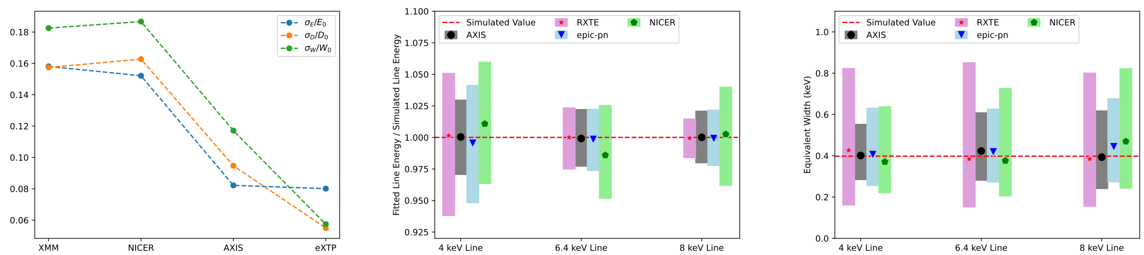

Figure 13. *Left Panel:* Results of quiescent magnetar phase-resolved spectroscopy simulations as average percent errors (i.e. 1σ errors divided by the fitted parameter value) for line energy (in blue), line depth (in orange) and line width (in green) for various telescopes. Simulations were conducted based on the models and parameters in [290]. *Middle and Right Panels:* Average fitted per simulated line energy (*Middle)* and fitted line width (*Right)* for three line energies simulated based on the original 6.4 keV burst spectral line detection of SGR 1900+14 in [283]. Error bars reported are 1σ parameter errors averaged over 100 iterations. Red dotted lines indicate simulated values.

5.4. Summary

Isolated neutron stars have been intensely studied during the previous decades by X-ray observatories, which have significantly improved our understanding of neutron stars. However, there are still a lot of things that are not well understood. As we demonstrated above, AXIS will discover more neutron stars and characterize their emission properties accurately, enabling meaningful population studies from which a unification of the neutron-star classes may be achieved. Although not detailed above, AXIS studies of individual neutron stars will also help in understanding physics under extreme conditions; e.g., accurate measurements of the spectra of CCOs and XDINSs can reveal the nature of the absorption features (cyclotron *vs* atomic transition) commonly seen in CCOs and XDINSs. With AXIS, such features may be found from more isolated neutron stars in different classes [e.g., like one in SGR 0418+5729; 291]. As demonstrated here, AXIS will deepen our understanding of isolated neutron stars in many ways.

6. Compact Objects: Accretion-Powered Compact Objects

6.1. X-ray binaries

The AXIS Galactic plane survey will represent a leap forward in understanding the population of X-ray binary systems in our Galaxy.

6.1.1. LMXBs

Jonker et al. [143] estimated that within the footprint of the Chandra Bulge survey, which covered 12 square degrees, that there was a population of approximately 530 LMXBs (the vast majority of which were in quiescence). Assuming a similar space density throughout our GPS footprint, we believe the AXIS Galactic plane survey should observe a field containing 2000-3000 LMXBs. As noted in Jonker et al. [143], the mean x-ray luminosity of quiescent LMXBs (qLMXBs) is around $10^{3}3$ erg/s, and their survey depth was optimized such as to be sensitive to about half of these sources. With a depth of 3×10^{-15} erg/s, the AXIS GPS would completely detect the hypothetical population of LMXBs presented in the Jonker et al. [143], including all those below the detection threshold of the Chandra Bulge survey. Additionally, the bright half of sources would be detected with high significance, allowing for high-quality spectral characterization, as well as time domain studies of the x-ray variability in these sources. Because the AXIS GPS will be a cadenced survey conducted with on the order of ten epochs spaced out over 5 years, we also expect to be sensitive to X-ray transients, which may allow for the detection of outbursting LMXBs which elude all sky X-ray monitoring facilities.

6.1.2. UCXBs

In addition to being a powerful facility for identifying ultracompact accreting white dwarf binaries, we expect the AXIS Galactic plane survey footprint to host 2000-3000 ultracompact x-ray binaries with BH/NS accretors based on the densities presented in Jonker et al. [143]. Notably, these systems have an order of magnitude lower luminosity in their quiescent states than longer-period UCXBs, making the sensitivity of the AXIS GPS survey a particular asset in identifying these systems. Many such systems may undergo eclipses in the optical (as the disk is occulted by the donor), and thus cross matches of the AXIS GPS point source catalog with surveys such as Roman and LSST could be a powerful way to identify these rare systems. Additionally, some of these systems, like their white dwarf binary counterparts, will be luminous in millihertz gravitational waves, and will be detected by LISA. Thus, AXIS could be used to provide rapid localization of the GW source by significantly cutting down on the number of possible electromagnetic counterparts (since most of these sources will be undergoing stable mass transfer, and thus are likely to exhibit a positive pdot in LISA, indicating that one should look in the x-ray to find the counterpart). Additionally, the AXIS GPS and deep surveys of globular clusters may directly reveal more rare UCXBs via periodicity searches in the x-rays, such as the candidate 28 minute orbital period BH+WD UCXB, 47 Tuc X9 [21].

6.2. Ultra Luminous X-ray Sources

A large number of XRBs with luminosities that exceed 10^{39} erg/s have been discovered in nearby galaxies. These are commonly referred to as Ultra-Luminous X-ray sources [ULXs, see recent review; 162]. It has been speculated that ULXs offer evidence for the existence of intermediate-mass BHs (IMBHs, with $M \sim 10^2 - 10^4\ M_\odot$; [56]). Alternatively, ULXs can be products of super-Eddington accretion onto a stellar-mass compact object [264]. The latter scenario has been favored by the presence of photoionized nebulae around ULXs that may be naturally explained by strong outflows combined with the large intrinsic X-ray luminosity [245,276,278]. More specifically, theoretical models for ULXs invoke super-critical accretion discs, where advection and outflows play a key role in shaping the disc structure. However, the smoking gun for super-Eddington accretion was the discovery of pulsations from M82 X-2, a system with luminosity of $10^2\ L_{\rm Edd}$, demonstrating that stable accretion onto NSs at super-Eddington rates is possible [17]. This discovery introduced a new category of systems, the so-called Ultra-Luminous X-ray Pulsars (ULXPs). This realization has fueled a search that led to the discovery and study of more ULXPs in recent years [e.g., 41,85,139,255,261]. Furthermore, based on spectral similarities between non-pulsating and pulsating ULXs, there is now compelling evidence that a significant fraction of ULXs may actually host strongly magnetized NSs [$B > 10^{12}$ G; 165,309]. Based on surveys and efforts of multiple observatories more than 2000 ULX candidates are now known [e.g. 169,308]. However, apart from the ULXPs the nature of most of the other sources remains elusive. AXIS can help push forward the study of ULXs. Apart from the obvious increase in identified ULXs that will result from the increased effective area and reduced PSF size compared to current observatories (i.e. XMM-Newton, Chandra, Swift), AXIS will greatly increase our understanding of the known ULXs in both spectral and timing properties.

In terms of spectral studies of ULXs AXIS can deliver up to 4 times more counts than XMM-Newton, while due to more flexible pointing capabilities monitoring surveys of nearby galaxies (like M51) could enable study of spectral variability of ULXs during super-orbital and/or outburst cycles [e.g. 106,176,177]. ULXs also exhibit long-term variability that sometimes can be quasi-periodic and related to some precession of the system [e.g. 62,167,176], while other systems might show sudden drops in flux that may be related to propeller transition and thus be evidence of magnetized neutron stars [189]. AXIS observations during low flux phases of ULXPs would enable tests of the mechanism behind these transitions in more systems.

Meanwhile, the timing resolution of AXIS (i.e. smaller than 0.2 s) would be enough to search for pulsations from many more ULXs, or track the spin evolution of ULXPs. We note that most ULXPs have spin periods close to 1-3 s, with very low pulsed fractions (10-20%). The exception is NGC 300 ULX-1 where its spin period evolved between 126 s to 16 s within a couple of years, while its pulsed fraction was more than 50% [301]. To quantify the capabilities of AXIS for such timing studies, we performed simulations on the ULXP source M51 ULX-7, a 2.8s pulsar on a 2-day binary system located in the outskirts of the spiral galaxy M51a at a distance of 8.6 Mpc [255]. Moreover, the flux of the system varies between 1-10$\times 10^{39}$ erg/s, showing a super-orbital modulation with a 40 d period and some evidence of propeller transitions [302]. Based on archival XMM-Newton observations, pulsations are not always visible and pulsed fraction is on the order of 10-15%. With AXIS, we could detect about 3.5 times more counts in a single visit compared to XMM-Newton, while the background contamination (due to diffuse emission and other point sources in M51) would be minimal compared to that in an XMM-Newton observation (20% or even more in counts). By performing simulations we found that assuming a pulsed fraction of 0.2, pulsations would be detected with as little as 5000-7000 counts which may be collected in a 10-20 ks AXIS observation throughout the super-orbital modulation. The major advantage of AXIS would be that the spin period would be detected in a fraction of the orbital period, thus pulsations would not be smeared by the Doppler effect. In contrast, the search for pulsations with XMM-Newton would require exposures over 100 ks, and would require acceleration searches [255].

6.3. Super Soft AGN

Super Soft Active Galactic Nuclei (SS AGN) are soft X-ray excess dominated AGN [183,269]. They are identified by very steep X-ray spectra (photon index $\Gamma > 3$) and high X-ray luminosities ($L_X > 10^{41}$ erg s^{-1}) [286]. They host higher-mass intermediate to lower-mass supermassive black holes with $M_{\rm BH} \sim 10^4 - 10^6 M_\odot$ [257] and are likely to be the missing link between the ULXs and normal AGN. Sacchi et al. [257] identified and confirmed only five such AGN from the *XMM-Newton* catalog of serendipitous sources [4XMM-DR9, 315]. The AXIS deep sky surveys will significantly increase the current sample size of SS AGN.

SS AGN emit X-ray photons predominantly below 2 keV. It is thus unknown whether they intrinsically lack the hard X-ray emission or the current X-ray telescopes are not sensitive enough to detect the weak hard X-ray emission from the corona. For a given radius, the inner disk temperature of SS AGN is higher compared to typical AGN disks, which could potentially impact the coronal geometry and/or emission properties of SS AGN. Thus the high sensitivity of AXIS will be crucial in determining the true nature of hard X-ray emission and corona in SS AGN.

6.4. Super Soft Sources

First discovered in the Magellanic Clouds by the Einstein Observatory (HEAO-2)'s early exploration of the X-ray sky (see figure 14 for the currently known LMC population), the class of objects we now call supersoft X-ray sources (SSSs) are classified by their very soft, blackbody-like spectra (with kT $\sim$ 20–100 eV) and luminosities ranging from 10^{35}–10^{38}erg/s [102,103]. Based on this energy release and their inferred radii, these objects were identified as accreting white dwarfs undergoing nuclear-burning near their surface [146,299]. It was soon found that within a narrow range of accretion rates (≈ 1–$4 \times 10^{-7} M_\odot/yr$, consistent with thermal timescale mass transfer) steady, persistent nuclear burning of all accreted material was possible. Above this range, optically-thick winds may drive an outflow [108] and on longer timescales, re-inflate the white dwarf envelope to giant dimensions [43]. For accretion rates below the steady-burning

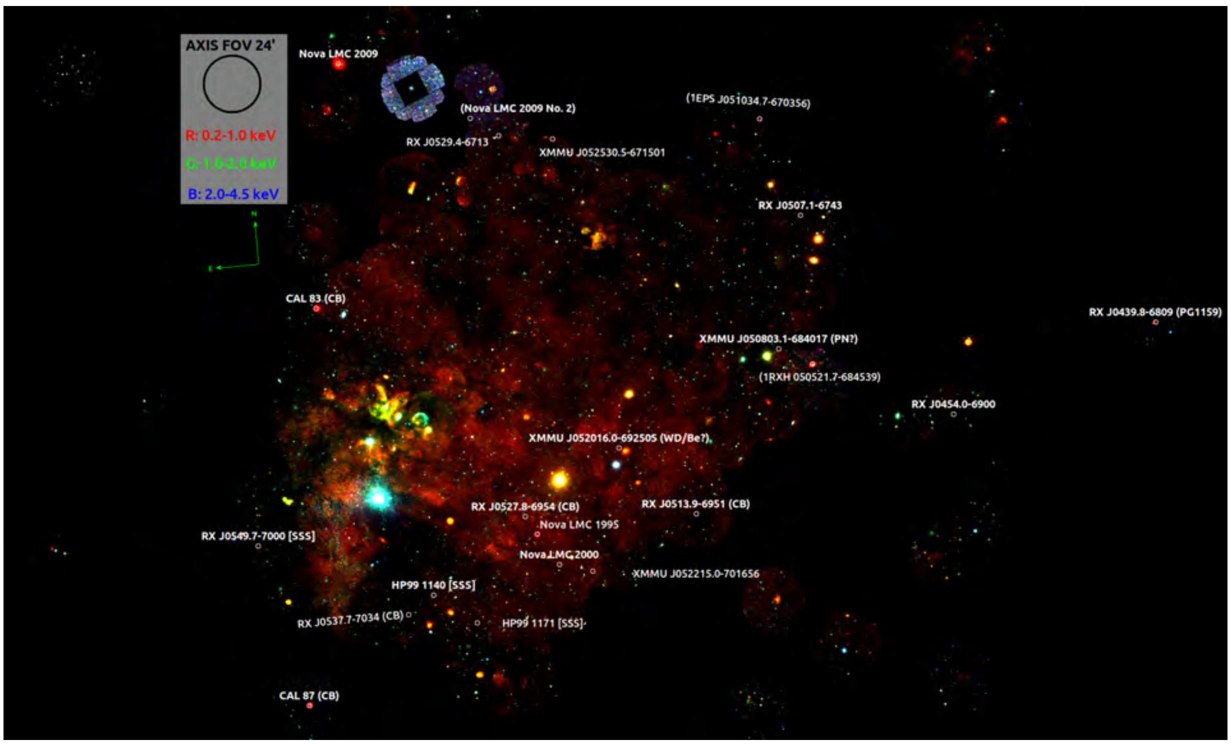

Figure 14. X-ray mosaic image (Red:0.2-1.0 keV, Green:1.0-2.0 keV, Blue:2.0-4.5 keV) of the LMC based on XMM-Newton observations (credit: XMM-Newton Large survey of LMC, PI F. Haberl). Regions mark the known close-binary supersoft sources in the LMC, while diffuse soft X-ray emission (i.e. <1 keV) is evident throughout the galaxy. Axis field of view (24′ diameter) is also marked in the plot.

threshold, matter accumulates in the partially degenerate envelope until triggering a thermonuclear eruption, giving rise to classical and recurrent novae [e.g., 47,247]. Following the nova outburst, an accreting white dwarf may sustain a post-nova supersoft phase whose duration depends on the mass of the WD and the rate at which it's accreting [275].

It is possible that supersoft X-ray sources are, instead, powered by super-Eddington dynamical timescale/unstable mass transfer onto a stellar-mass black hole or neutron star companion, prior to common-envelope event. In such scenarios, the powerful outflows accompanying the rapid mass transfer will inflate a compact, radio-synchrotron-bright "hypernebula" [276]. The dense disk outflows do not allow the disk photons to emerge directly from the disk surface, instead, they emerge after multiple scatterings from the fast wind/jet photosphere at much larger radii. This reduces the effective temperature of the disk emission to 10$\sim$100 eV thus enabling hypernebulae to be candidates for ultraluminous supersoft X-ray sources. These sources, if jetted, could be sources of fast radio bursts if the jet is pointed along our line of sight [277]. Furthermore, the protons accelerated at the jet termination shock of hypernebulae could interact with the beamed soft X-ray disk photons and produce high-energy neutrinos. Integrated over volume and time, this could potentially make SSSs one of the significant contributors to the background extragalactic high-energy neutrino flux as seen by IceCube [278].

SSSs have received intensive scrutiny due to their possible role as progenitors of Type Ia Supernovae (see above), as well as the role novae [90] and rapidly-accreting white dwarfs [67] may play in the origin of the elements. Accreting white dwarfs also provide a vital benchmark in our understanding of the stability and evolution of mass transfer in binary stars, and in particular, the possible mechanisms underlying the mysterious common envelope phase, a vital step in the formation of virtually all compact binaries and gravitational wave sources. This closely links the understanding of SSSs with the goals prioritized by the Astro2020's Report of the Panel on Stars, the Sun, and Stellar Populations, in particular:

G-Q2: "How does multiplicity affect the way a star lives and dies?"

Making progress on understanding the still-little-understood formation, evolution, and ultimate fate of SSSs will require extraordinary **sensitivity in the soft X-ray band**, superior **angular and timing resolution**, and **dedicated monitoring** campaigns working in synergy with surveys in other wavebands. This is an approach identified as particularly essential by Astro2020's New Messengers and New Physics priority, noting "*the power of near-continuous monitoring... in the X-ray, gamma-ray, optical, infrared, and radio bands has been dramatically demonstrated over the past two decades.*"

AXIS will provide an absolutely essential tool in unraveling these mysteries, driving forward our understanding of accreting white dwarfs across several orders of magnitude in accretion rates, as well as their behaviour on timescales from seconds to decades. Its relatively wide field of view and soft X-ray sensitivity will allow future guest observer programs on AXIS to quickly and efficiently map the SSSs of nearby stellar populations. Assuming a typical column density $N_H = 10^{21}\mathrm{cm}^{-2}$, and that a reliable spectral measurement of the effective temperature of a given source would require $\sim$200 counts, we find that AXIS will be able to detect any steady-burning SSS with a white dwarf mass above $\sim 0.8M_\odot$ in M31 within a 20ks exposure, and any such white dwarf above $\sim 0.55M_\odot$ in the LMC in a 1 ks exposure (see figure 15). At these depths, AXIS would be able to carry out a comprehensive survey of M31 in $\sim$18 pointings, and cover a broad swath of the central region of the LMC in $\sim$60 pointings, providing a powerfully complete census of both persistent and post-novae SSSs; repeating all or part of this campaign on an approximately annual basis would in turn provide an invaluable history of their long-term behaviour, resolving key questions such as the mechanism(s) underlying post-nova mass loss [319]; the true numbers of such objects & their possible role in some Type Ia supernova explosions [275]; and their role in the origin of i-process and other elements [67]. At the same time, monitoring short term pulsations observed in persistent and

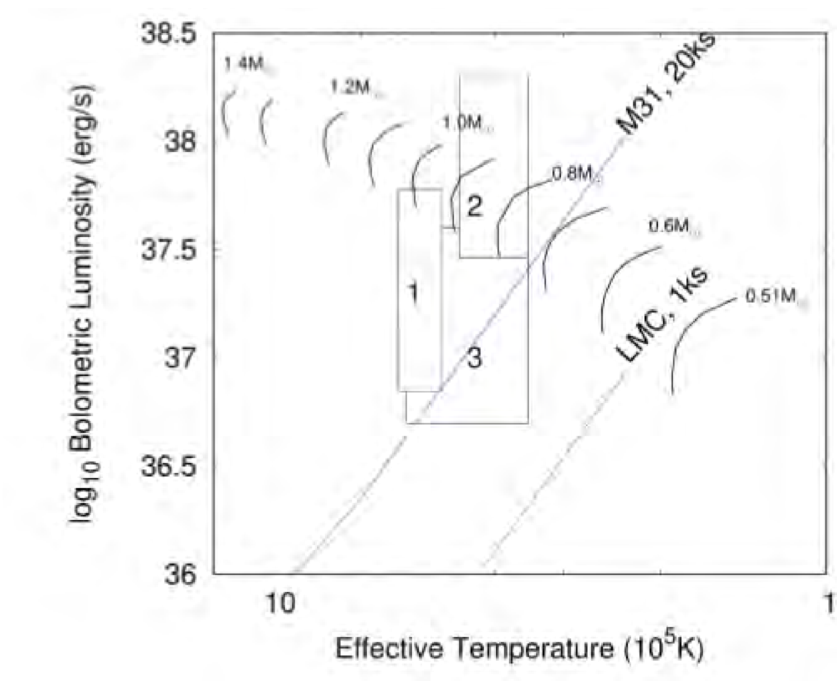

Figure 15. Detection limits for a given blackbody luminosity and temperature, assuming $N_H = 10^{21} cm^{-2}$ and two assumptions about distance and total integration time: 20ks for an object in M31 (blue line) and 1ks for an object in the LMC (red line). Solid black lines denote steady hydrogen-burning SSS models from [318]; black boxes denote approximate measured values for a selection of known close-binary SSSs with well-studied spectra — (1) 1E 0035.4-7230; (2) RX J0513.9-6951; and (3) CAL 83 [103,279].

post-nova SSSs (on timescales of 10's to 100's of seconds) can disambiguate whether these pulsations are driven by g-mode oscillations in the outer envelope [211,319] or are instead evidence of a rotating hot spot on the white dwarf surface [see, e.g., 211,303, for further discussion], in either case potentially providing a novel means of inferring the mass and possible growth of the accreting white dwarf, and the physics underlying its continued accretion. Looking further afield, AXIS observations of nearby spiral galaxies would provide an invaluable probe of SSS evolution while complementing a host of ancillary Galaxies science, from understanding stellar and black hole feedback to the physics of the circumgalactic medium. In particular, $\sim$200ks total exposures following-up the Chandra Survey of Nearby Galaxies (11 galaxies at distances of $\sim$4–13Mpc) [161] supplemented by, e.g., additional objects from the PHANGS survey [173] could provide a comprehensive census of the most massive accreting nuclear-burning white dwarfs (i.e., those closest to the Chandraskehar mass) in a range of environments spanning different star formation histories and metallicities. These results are vital to our emerging picture of the evolution of Type Ia supernova progenitors over cosmic time, and a critical test of our understanding of binary stellar evolution in the local Universe.

Fundamental to the discovery potential of AXIS in uncovering the evolution of accereting compact object populations will be its strong synergies with other great observatories of the next decade, as well as ongoing efforts today. With its relatively wide field of view and high angular resolution, AXIS will be uniquely well-matched to the Cosmological Advanced Survey Telescope for Optical and uv Research (CASTOR), a proposed 1m UV-optical space telescope with 0.15" resolution and $\sim$0.25 square degree field of view that will reach AB$\sim$27 in $\sim$600s, as well as providing grism and multi-object spectroscopy, planned for launch by the end of the decade [59]. Together, CASTOR and AXIS would provide an ideal combination for complementary surveys in UV & X-rays of nearby binary populations, especially in crowded fields; enable multi-wavelength fitting of close binary supersoft source spectra; and allow monitoring of massive companions of HMXBs & accretion disks. With both missions anticipating dedicated surveys of the galactic plane, and likely the LMC and M31 as well, CASTOR and AXIS would provide a uniquely powerful pairing. By leveraging the results of presently ongoing deep, multi-epoch spectroscopic surveys, in particular the Sloan Digital Sky Survey (SDSS)-V [166], AXIS could further probe the role that accreting compact objects may play in contributing to the ionizing background in galaxies [320,321].

7. Pulsar Wind Nebulae

Pulsar-wind nebulae (PWNe) harbor one of the most extreme particle accelerators known to exist in the Galaxy – young rotation-powered pulsars powering ultrarelativistic magnetized winds (see [86,148,254]). Studies of synchrotron emission, dominating PWNe spectra from radio to MeV gamma-rays, provide a window into the inner workings of these remarkable relativistic magnetized plasma laboratories. In particular, high-resolution X-ray images and spatially resolved spectroscopy can elucidate the following aspects:

- collisionless shock physics in relativistic magnetized outflows (e.g., by resolving termination and bowshock morphologies and particle SED evolution);
- kinetic particle escape, conditions in ISM and its magnetic field, and propagation of ultrarelativistic particles in ISM, including the positron distribution in the Galaxy;
- magnetic reconnection and turbulence in magnetized plasma;
- particle acceleration mechanisms operating in relativistic magnetized outflows and pulsar electrodynamics (e.g., pair cascade physics and spin-dipole axis alignment);
- supernova explosion physics leading to neutron star kicks and misalignment between the pulsar spin and magnetic axis;
- massive star evolution by establishing the progenitors of RRPs through establishing connections between pulsars and properties of their host SNRs.

The morphologies and spectra of PWNe [151] depend on the anisotropy of the wind, its magnetization, particle acceleration efficiency, magnetic field strength, and pulsar velocity. These intertwined dependencies can be disentangled by (1) resolving the PWN structure, (2) connecting PWN properties with the pulsar properties and the ambient medium properties (including the host SNR), and (3) increasing the number of PWN detected in X-rays to enable meaningful population studies.

While many pulsars have reliably measured spin-down energy loss rates ($\dot{E}$), it is much more difficult to determine some other important parameters potentially influencing the morphologies, radiative efficiencies, and spectra of PWNe. Two of these, the angle ζ between the pulsar's spin axis and the observer's line of sight and the inclination angle α between the spin and magnetic dipole axes (if the field is indeed largely dipolar). are notoriously difficult to measure. These angles can be constrained by comparing theoretical models of pulsar magnetospheric emission with the *Fermi* LAT GeV light curves and radio light curves (e.g., [45,226,314]). However, different magnetosphere models can give differing predictions. Since pulsar winds are intrinsically anisotropic many PWNe exhibit prominent equatorial and polar components (e.g., tori and jets) which reflect symmetry with respect to the pulsar spin axis (see, e.g., the Crab and Vela PWNe in Figure 16). Resolving these PWN features often allows one to identify the symmetry axis (rotation axis) and, hence, ζ (see [212,213]). Independent determination of ζ breaks the degeneracy between the models and helps to determine the one which is consistent with the data. Some PWNe display nearly-axial symmetry, but identifying the equatorial and polar outflows can be challenging (e.g., G21.5–0.9 and MSH 11–62 in Figure 16). The anisotropy of pulsar winds can lead to anisotropic PWN spectra, flow speeds, magnetic fields, and cooling trends, requiring high-resolution imaging, spatially-resolved spectroscopy, and spatially-dependent models accounting for wind anisotropy. It is plausible that the lower values of α would result in a highly magnetized wind with a stronger polar outflow (compared to the equatorial torus) and also perhaps a reduced particle acceleration efficiency and lower PWN luminosities (see modeling by [36]). However, a larger sample of PWN with spatially-resolved morphologies and spectra is needed to perform informative population studies and test theoretical predictions for models of relativistic magnetized outflows from pulsars.

The most telling sign of the acceleration mechanism is the slope (shape) of the SED of accelerated particles and its dependence on other (e.g., pulsar or ambient medium) parameters. However, pulsar wind particles suffer radiative energy losses causing changes causing the evolution of the SED with the distance from the pulsar. Therefore, to determine the particle spectral energy distribution (SED) injected at the TS, one must obtain spatially-resolved PWN spectra (see Figures 16-17 and 19 and [104]).

The "natal kicks" that pulsars receive in supernova explosions lead to high pulsar velocities with the average $v_{\rm psr} \sim 400$ km s^{-1} [130]. This implies that most pulsars remain inside their host SNRs only for a few tens of kyrs and then escape into the interstellar medium (ISM) where the speed of sound $c_{\rm ISM} \ll v_{\rm psr}$ (typically, $c_{\rm ISM} \sim 3 - 30$ km s^{-1}, depending on the ISM phase). Therefore, in the ISM the pulsar motion becomes supersonic (Mach number $\mathcal{M} \equiv v_{\rm psr}/c_{\rm ISM} > 1$), and the ram pressure from the oncoming ambient medium strongly modifies the PWN appearance leading to the formation of extended pulsar tails (see [153,254] for reviews on supersonic PWNe). Although in supersonic PWNe the structures formed by the anisotropic wind (e.g., jets and tori) are deformed by the ram pressure, in some cases, the torus-jet structure can still be identified in high-resolution images (see, e.g., J1509–5850, Geminga, B1706–44, and B0355+54 in Figure 2 of [153]).

In recent deep X-ray observations, a new type of structure has unexpectedly been discovered in some supersonic PWNe. Extended, elongated features, *strongly misaligned with the pulsar's direction of motion*, are seen originating from the vicinity of four pulsars (see Figure 20 for examples). The misaligned orientation of these features is surprising because for a fast-moving pulsar, one would expect all of the pulsar wind to be confined within the tail (which these PWNe exhibit as well). A hypothesis where relativistic particles populating the misaligned features escape from the compressed apex of the bowshock,

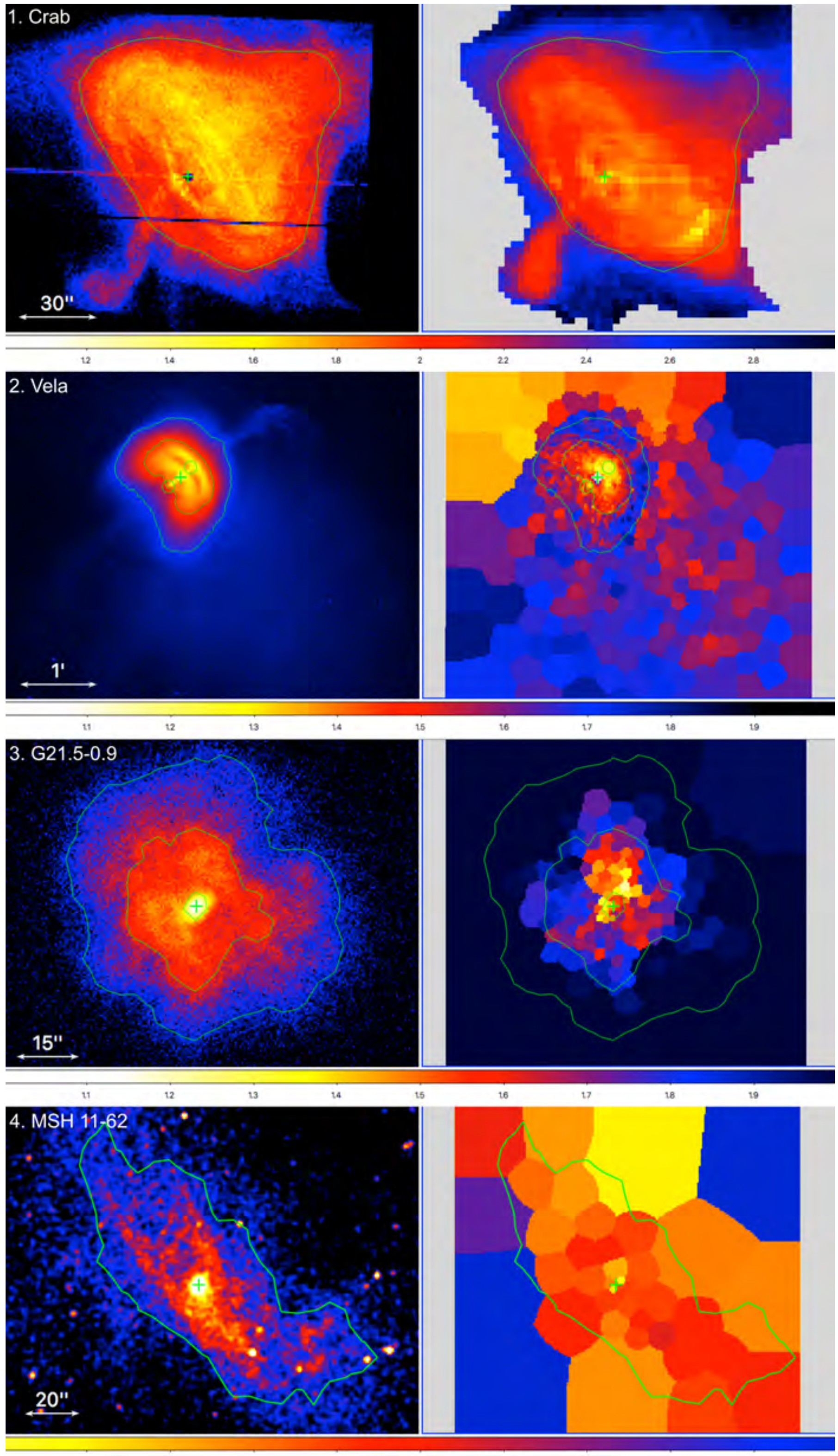

Figure 16. *Left panels:* Chandra ACIS images (in 0.5–8 keV) of bright, well-resolved PWNe from table 1. *Right panels:* Adaptively-binned spatially-resolved spectral maps for the PWNe shown on the left. The color bars represent the photon index Γ measured in the 0.5–8 keV band. The green contours are shown for illustrative purposes, and the green crosses mark the pulsar positions. The gray-colored areas in panels 1 and 2 were excluded from mapping. The Crab spectral map is adopted from [**?**]. Adopted from [149].

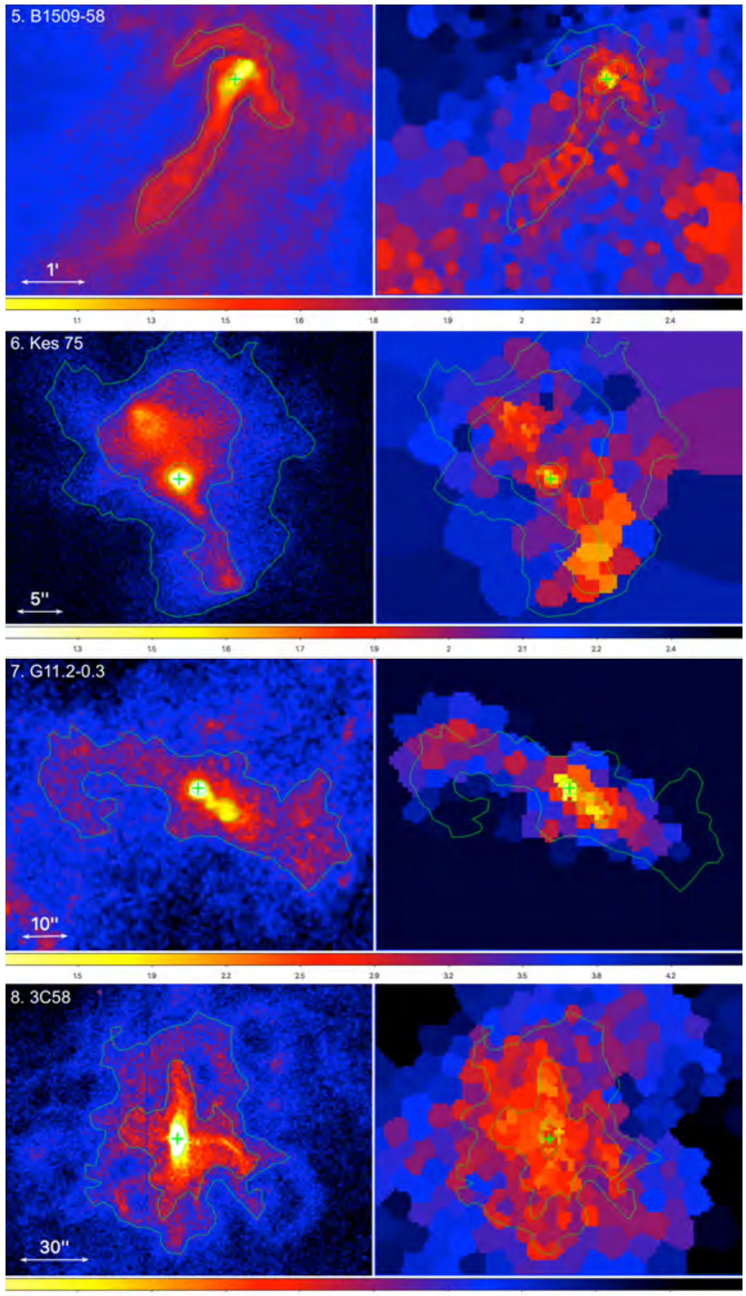

Figure 17. Chandra ACIS images and spectral maps of bright, well-resolved PWNe (continued from Figure 16). Adopted from [149].

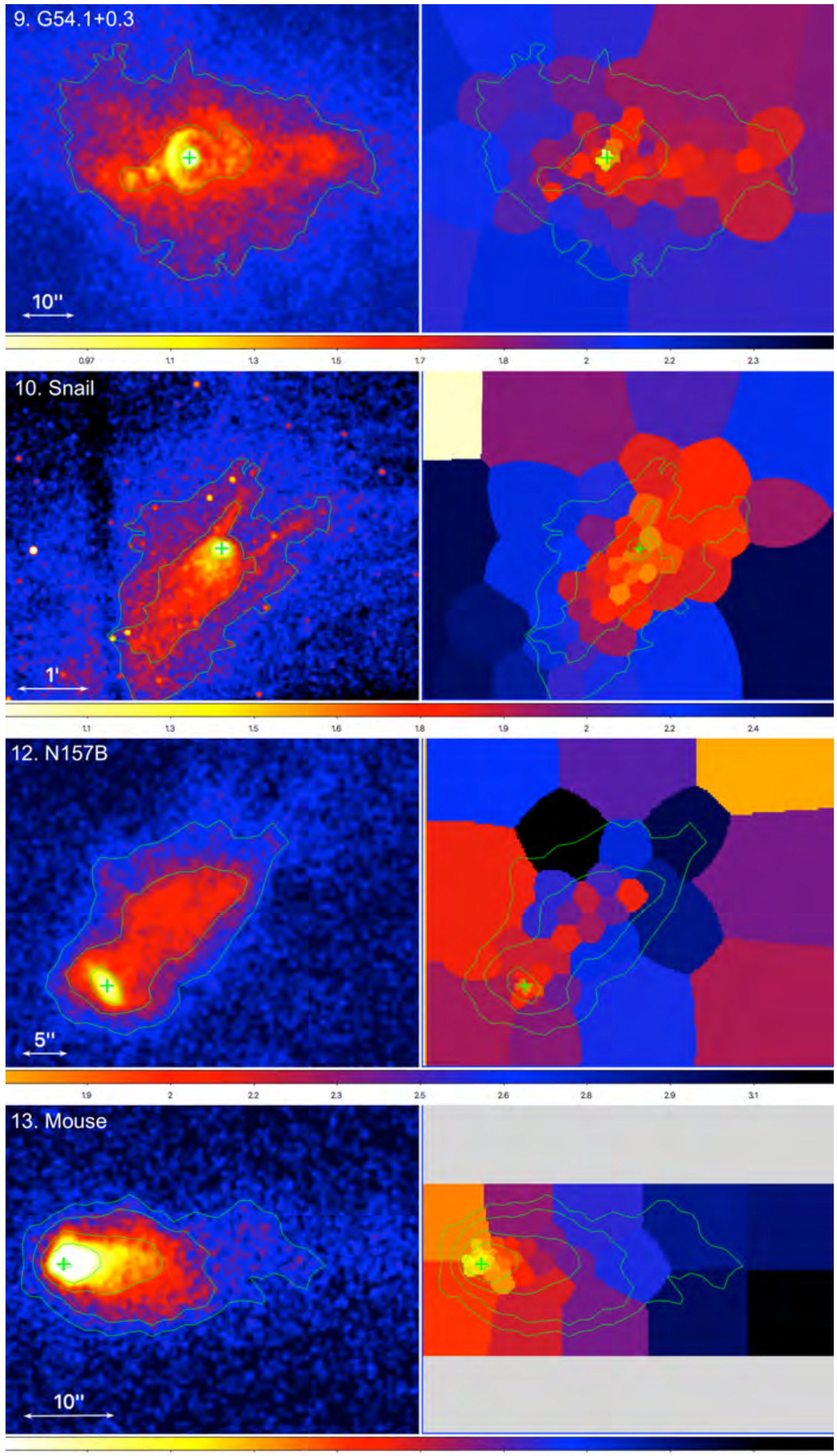

Figure 18. *Chandra* ACIS images and spectral maps of bright, well-resolved PWNe (continued from Figures 16 and 17). Adopted from [149].

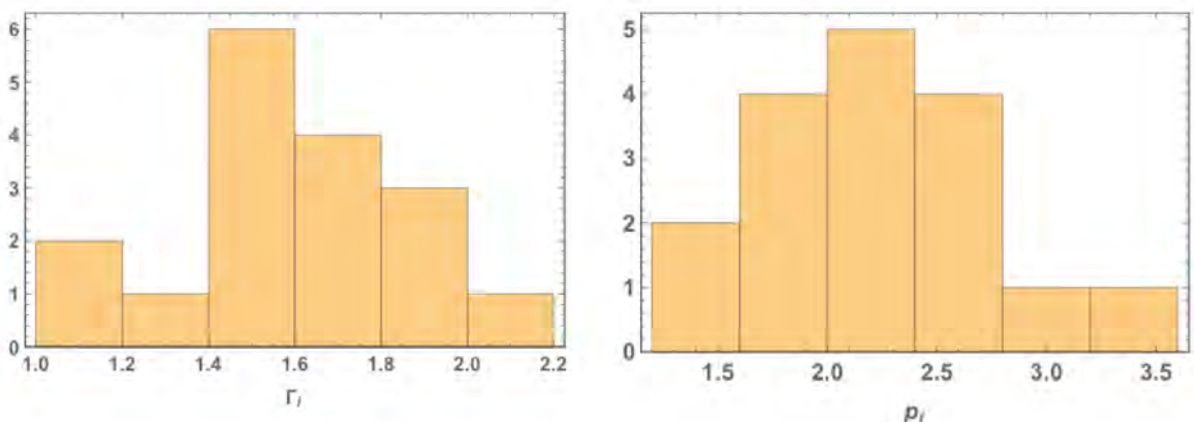

Figure 19. Histograms of $\Gamma_{\rm i}$ and $p_{\rm i} = 2\Gamma_{\rm i} - 1$ for the 17 PWNe listed in table 2 (note that pulsars 11 and 14 are omitted from table 2; see the caption). The bin width corresponds to the average measurement uncertainty. Adopted from [149].

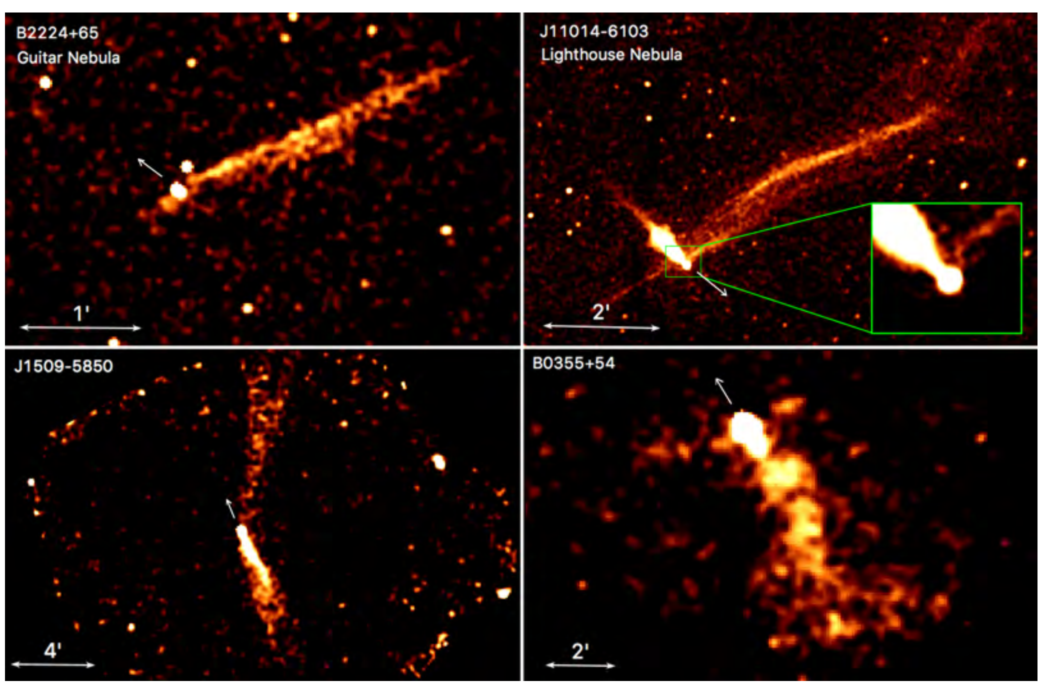

Figure 20. *Chandra* ACIS images of supersonic PWNe displaying tails and misaligned outflows. The white arrows show the directions of pulsar's proper motion. Adopted from [153].

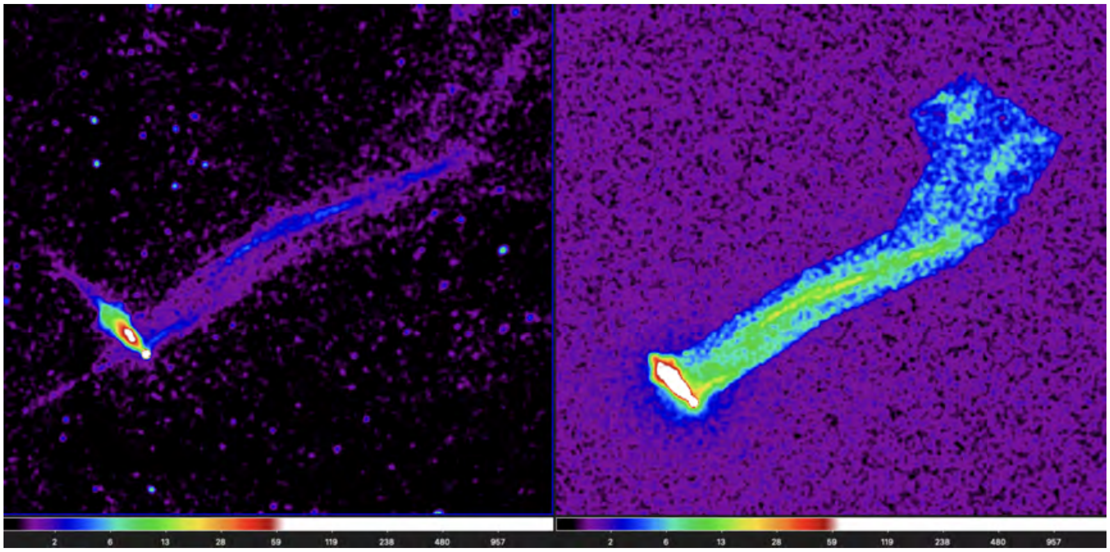

Figure 21. *Left: Chandra* image of the Lighthouse PWN featuring the brightest misaligned outflow (300 ks). *Right:* AXIS simulation (300 ks) created using `sixte` (with the *Chandra* image as input. The scalebar is in units of counts arcsec^{-1}. With the same exposure time, AXIS will collect ≈ 8 times more counts than *CXO*. Note, that with $1''$ PSF FWHM AXIS can recover all structures indicated by CXO observations within the extended outflow. It will also resolve the morphology of the compact PWN (tail and the head where the extended outflow originates as two faint streams).

where magnetic field reconnection can help the escape, has been put forward by [23] and further developed by [25] and [218]. It is important to stress that in this scenario the misaligned outflows are an entirely kinetic phenomenon, which makes them very different from the pressure-confined jets of tails. Since only the most energetic particles are expected to escape from the bowshock apex one test of this hypothesis would be the absence (or weakness) of the cooling (spectral softening) along the extended misaligned features. This kind of signature can be efficiently probed with AXIS for the brightest structures (e.g., the Lighthouse nebula; see Figure 21). The observed appearances of the misaligned outflows should reflect the ambient ISM structure[2] illuminated by synchrotron emission from the leaked pulsar wind particles. Thanks to its sensitivity and large field of view, AXIS is expected to discover more of these remarkable structures around fast-moving pulsars elucidating ultra-relativistic particle (including positrons) escape and transport in the ISM.

A related topic is the extended (with scales of tens of pc) TeV halos (also dubbed relic PWNe) discovered recently by Cherenkov imaging telescopes around some middle-aged pulsars. Due to their large extent, these TeV sources often include alternative possible sources of relativistic particles (such as SNRs and XRBS) but the leading hypothesis is that the TeV emitting particles are pulsar wind particles which mostly have cooled too much to detect their synchrotron radiation in X-rays, but the up-scattered (by the IC mechanism) background radiation is still seen in TeV, owing to a longer cooling time for this process. Sensitive observations with AXIS may pick up the faint synchrotron emission for PWNe associated with the pulsars powering TeV halos and reveal the expected fading with the distance from pulsar due to the radiative cooling. Such observations will be highly synergistic with radio and TeV observations from

[2] If the leaking particles carry sufficiently large currents, the currents can perturb the original ambient ISM magnetic field.

upcoming SKA and CTA by allowing to map out the evolution of the entire multiwavelength SED of the relic PWNe and enabling direct comparison with the particle transport model predictions.

AXIS's excellent angular resolution and large effective area combined with the low detector background make it possible to resolve (spatially and spectrally) the complex anisotropic structures of PWNe, such as bow shocks, wisps, knots, rings, jets, arcs and combinations thereof (see Figures 16–18). On larger scales ($\sim$0.1–10 pc), AXIS can resolve structures such as long diffuse tails directed opposite to the pulsar's motion, and strongly misaligned (with the pulsar's direction of motion) extended outflows (see, e.g., Figure 21 and Figure 9 in [153]).

In summary, the PWN study strategy for AXIS can be twofold:

- Deep observations of a relatively small sample of bright and large PWNe (most of which have been already studied with CXO) with the goal of obtaining high-quality images and spatially-resolved spectra (see examples in Figures 16–18).
- Searches of extended emission around young and middle-aged pulsars, as well as searches for non-thermal extended sources in the serendipitous galactic plane observations to increase the overall PWN population. The number of PWNe detected in X-rays approaches is of the order of 100 as of Sep. 2023 (ref. SNRcat). We expect that AXIS can double this sample by discovering new PWNe in X-rays and by following up on PWNe discovered in radio (e.g., with SKA, ngVLA, and their prototypes) as well as in TeV by CTA. The actual number will, of course, depend on the length of the mission operation.

8. Supernova Remnants

Supernova Remnants (SNRs) are among the most fascinating astrophysical objects in the Universe. They are the result of strong shocks and create a high-temperature low-density plasma out of interstellar gas and the stellar ejecta, impact the chemical enrichment and evolution of galaxies, accelerate cosmic rays to extremely high energies, and those resulting from core-collapse explosions make the most magnetic, compact, and dense objects in the Universe: neutron stars (NSs) and black holes. These plasma and compact objects are the best laboratories to study extreme astrophysics that cannot be achieved even in the most extreme particle accelerators on Earth, as well as relativistic outflows and jets that are ubiquitous in Astrophysics (see sections elsewhere). These objects have not only driven scientific breakthroughs, technology development and interdisciplinary connections, but they also fascinate the public and young people. To date we know of some 400 SNRs in our Galaxy, many of which have been imaged and studied in detail in the X-ray band, thanks to modern observations with Chandra and XMM-Newton; see SNRcat [80][3] for the high-energy, regularly updated, public database of SNRs, PWNe and associated compact objects. The past decade has in particular helped address many questions related to their formation and evolution; however our studies of SNRs have been limited to the brightest or closest objects to us, and we have so far touched only the tip of the iceberg. AXIS, thanks to its unprecedented sensitivity in the 0.5–10 keV band, excellent PSF over a large FoV, and low background will enable us to dramatically increase the population of faint SNRs in our galaxy and nearby Universe, and through targeted observations, tackle some of the most fundamental outstanding questions in the field that are relevant to Astro2020. Some of these pressing questions are highlighted below.

Note on Fig. 22: The total number of SNRs in the Galactic Plane Survey coverage is 50: 1 candidate, 17 composites, 2 filled-centre and 30 shell-type. The total number of SNRs in the bulge = 9: 3 composites,

---

[3] http://snrcat.physics.umanitoba.ca/

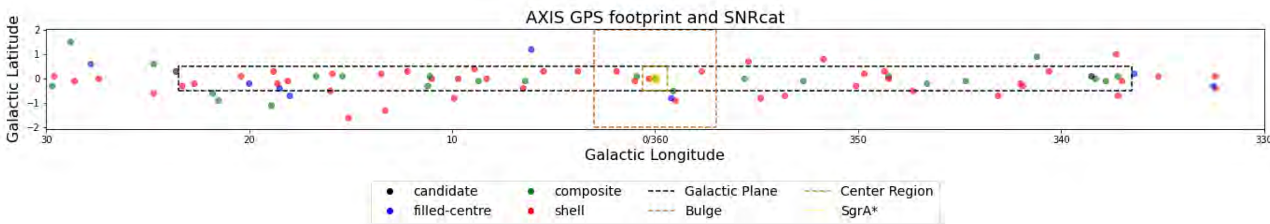

Figure 22. The known Supernova Remnants and Pulsar Wind Nebulae (from the High-Energy Catalogue of Supernova Remnants, SNRcat[4]) covered within the AXIS GPS footprints. Shells are shell-like remnants, Filled-Centres are PWNe or plerions, Composites have both a shell-like and a centrally filled component and include both plerionic and thermal Composites. Candidate SNRs and PWNe are included.

1 filled-centre and 5 shell-type. The total number of SNRs in the Galactic Centre is 2: 1 composite and 1 shell-type.

What are the progenitors and explosion mechanisms of supernovae?
A fundamental outstanding question about the evolution of massive stars is which stars make neutron stars and which ones make black holes. Among the core-collapse explosions that make neutron stars, there is a diversity that leaves behind a zoo of engines as described in SectionX.Y. For Type Ia SNe, commonly used as standard candles for cosmology, there is an ongoing debate about their explosion mechanism and aftermath: single degenerate versus double degenerate (see Section X.Y); and for some type Ia double-degenerate models, the white dwarf can survive the explosion leaving imprints in the supernova remnant for thousands of years after the explosion (e.g. Ferrand et al. [81]). Supernova remnants are ideal targets to probe the physics and aftermath of SN explosions: they provide us with a nearby laboratory to directly probe the compact engines and the supernova ejecta which can glow in the X-ray band for tens of thousands of years post the supernova explosion.

8.1. Mapping SNRs to their SN progenitors

SNRs are the primary sources of products of stellar and explosive nucleosynthesis. Nucleosynthesis is a rich, complex field that involves many disparate processes operating in different environments and at different phases of stellar evolution. Observational tests of specific model components, especially of the most energetic processes, are lacking. In particular, the processes that produce Fe and Fe-group elements and eject them into the interstellar medium during the explosions of both core-collapse and thermonuclear supernovae are among the most poorly tested parts of the entire nucleosynthesis picture. Young SNRs ($\lesssim$10 kyr) are particularly crucial for probing the chemical elements produced through numerous processes that are being debated. X-ray studies in particular provide critical tests of the nucleosynthesis picture especially as regards the production of Fe-group and intermediate-mass elements in both core-collapse and thermonuclear SNe. In addition, since the production of the Fe-group elements is at the heart of these explosions, they offer critical insights into the explosion processes in supernovae.

X-ray observations of SNRs provide a powerful tool to type remnants, study their energetics/environment, and map them to their SN progenitors. The core-collapse remnants are believed to be the dominant producers of the α-elements C, O, Ne, Mg, Si, and S,although they do produce a broad spectrum of elemental species including the Fe-group. The final amounts of alpha-elements are proportional to the initial mass of the progenitor star and depend on the details of the nucleosynthesis

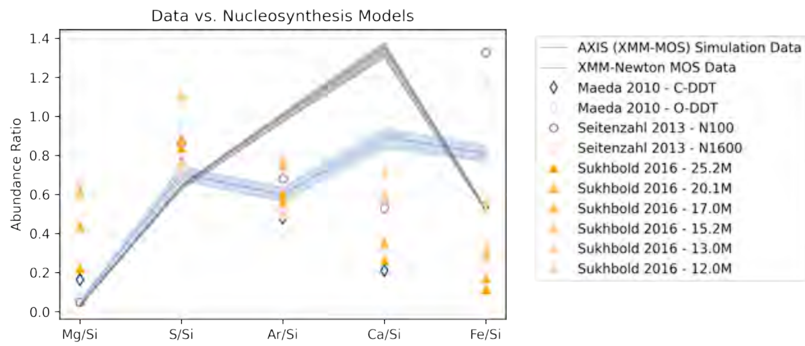

Figure 23

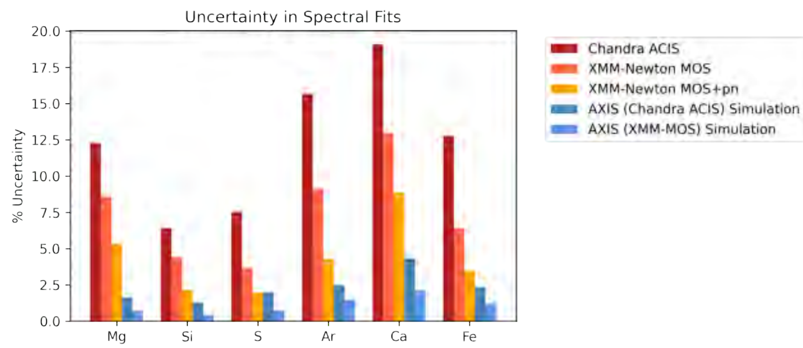

Figure 24

model assumed. On the other hand, the thermonuclear or Type Ia SNe are the dominant sources of Fe and the Fe-group elements in the Universe....

To add a section here on how spatially resolved spectroscopic studies of SNRs with Chandra and XMM-Newton are shedding light on the SN progenitor; however we need more sensitive spatially resolved studies to answer some of the quesitons in this field, particularly on connecting the zoon of neutron stars to the zoo of SN engines.

In a systematic study of SNRs in the Magellanic Clouds with XMM-Newton, a new class of evolved SNRs were discovered, which have an X-ray bright, Fe-rich core, consistent with reverse shock-heated Type Ia ejecta [32,158,159]. As the interior of such SNRs show bright Fe L emission around 1 keV, the X-ray color can be used to determine the type of the SN not only in the nearby SNR, for which one can perform studies of the morphology and the spectrum, but also in SNRs in further distant galaxies.

8.2. Probing Neutron Star kicks and their SN explosion mechanism

This section is being expanded on.

The origin of neutron stars' velocities (several hundreds km/s) is a long-standing mystery in astrophysics. There are two main competing mechanisms to neutron star kicks: (a) anisotropic ejection of the stellar debris (hydrodynamic kick, [140]) and (b) asymmetric-neutrino emission (neutrino-induced kick, [27,322]). Fortunately, the two scenarios predict a clear difference in the kick velocities and SN asymmetries. The hydrodynamic kick mechanism predicts that neutron star velocities are directed opposite to the stronger explosion where explosively nucleosynthesis elements from Si to Fe are preferentially expelled, whereas the neutrino-induced kick mechanism either suggests no correlation between neutron star velocities and SN asymmetries, or predicts the strongest mass ejection in the direction of the neutron star's motion.

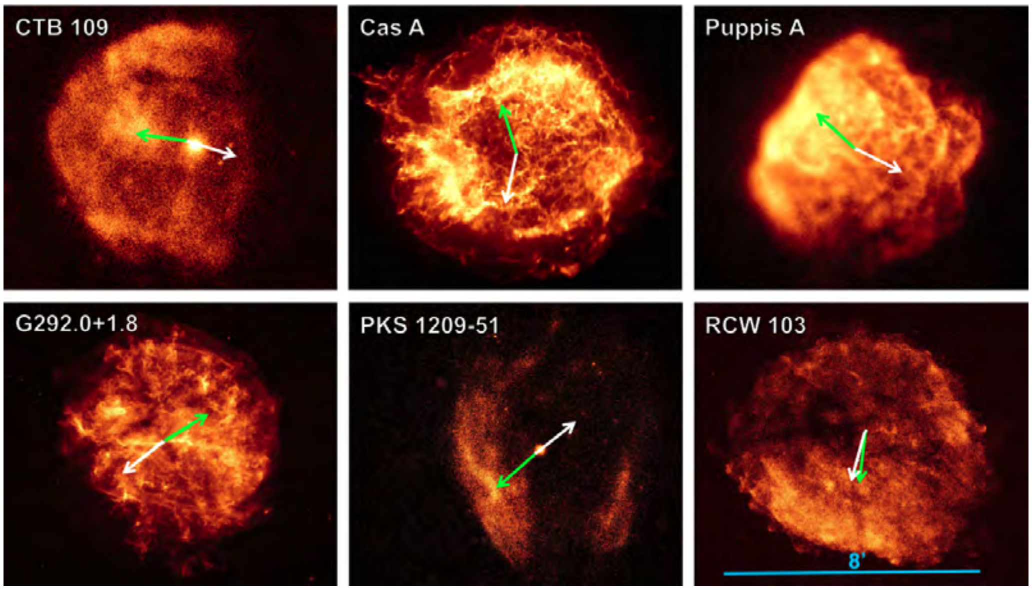

Figure 25. 0.5–-2.1 keV Chandra and ROSAT images of six SNRs for which there is a robust measure of their explosion sites. The green arrow points from the explosion site to the direction of the dipole moment. The white arrow points in the direction of the neutron star's motion. In Cas A and G292.0+1.8, the dipole moment direction reflects the bulk of ejecta emission. In CTB 109, Puppis A, and RCW 103, the dipole moment points toward enhanced emission that is due to interactions with CSM/ ISM or a molecular cloud. The scale shown in the last panel shows the SNR size which can easily fit within the 24′-circular diameter FoV of AXIS. Figure credit: [131].

Recent X-ray observations of SNRs revealed that neutron stars preferentially move opposite to the bulk of either X-ray emission [131] or intermediate-mass elements [157], supporting the hydrodynamic kick scenario. However, in many cases, neutron stars' velocities are indirectly inferred from displacements between their positions and geometric centers. The number of robust samples is still quite small and the sample includes a couple of outliers (see Fig. 25). AXIS will significantly increase the observational sample and is the most suitable mission suitable for tackling this science. The Chandra-AXIS baseline will provide the timescale needed to constrain the proper motion of neutron stars, while taking advantage of their matched angular resolution. At the same time, the unprecedented sensitivity of AXIS combined with its high angular resolution over the full SNRs hosting the compact objects will enable a much better constraint on the bulk of X-ray emitting ejecta.

8.3. Deciphering the SN environments through their shocks' proper motion

How do SNR shocks impact cosmic magnetism?

Turbulent magnetic fields at young SNR shocks are expected to be significantly amplified by a cosmic-ray current driven instability that develops in the shock precursor. Magnetic field amplification (MFA) is thought to be the key element in non-linear Diffusive Shock Acceleration (DSA) theory (see e.g., [37]). X-ray observations with *Chandra* have revealed the presence of narrow synchrotron X-ray filaments at the outer edge of young SNRs, demonstrating that the strong shocks at young SNRs are indeed capable of amplifying the interstellar magnetic field by large factors (e.g., [307]). The narrowness of synchrotron X-ray filaments could be due to rapid synchrotron cooling of high-energy electrons in the postshock flow if the magnetic field strength reaches ~ 0.1 mG. In some cases, time variability of the synchrotron X-ray flux can be seen, which is additional evidence in favor of magnetic field amplification [295].

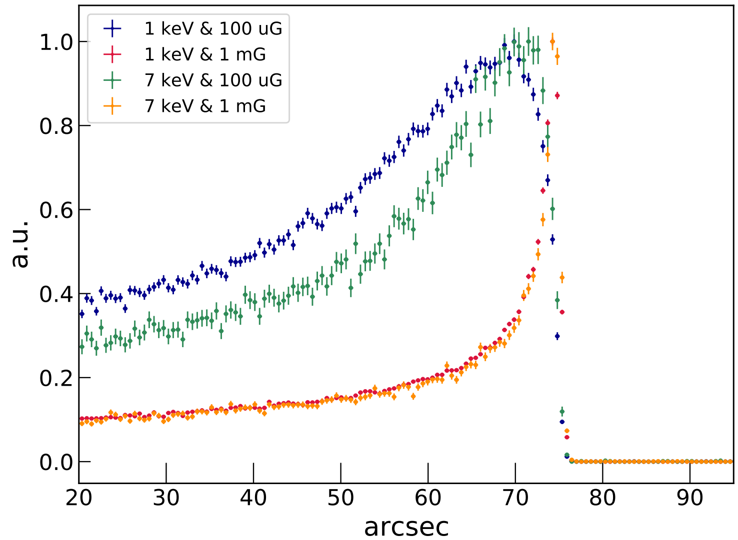

Figure 26. Simulated radial profiles of shocked emission from a young, 20 pc diameter SNR, at a distance of 1 kpc. The 100 ks AXIS simulations, for amplified magnetic fields of 100μG and 1 mG, illustrate that the shock narrows in width for stronger fields. *Will add another figure next showing the thin filaments.*

The turbulent magnetic fields, amplified most likely by CR current driven instabilities, can be imprinted in the spatial structures of the synchrotron X-ray filaments. Testing the theoretical predictions is best achieved with high-angular resolution measurements of the energy dependence on the width of the filamentary structures. The width of the shell depends on the magnetic field B, the energy of electron E_e and the corresponding synchrotron X-ray photon energy ε_X: $w \propto E_e^{-1/2} B^{-7/4} \propto \varepsilon_X^{-1/4} B^{-3/2}$ [**?**]. Figure 26 shows the radial profiles of the synchrotron X-ray filaments that are expected to be observed by *AXIS*. We can measure the energy dependence on the width of the synchrotron filaments thanks to the superb angular resolution of AXIS over a large field of view, thereby verifying the theoretical prediction. AXIS has the advantage of maintaining excellent angular resolution over the full SNR, while Chandra can generally only retain arcsecond spatial resolution over a small portion of the remnant.

Where are the missing SNRs in our Galaxy and beyond?
Elaborate here on Galactic and SMC/LMC/nearby galaxies SNR population studies.

The largest and actively star-forming satellite galaxies of the Milky Way, the Large and Small Magellanic Clouds (LMC, SMC) are ideal places to study SNRs due to their low foreground absorption and small distances of $\sim$50 kpc and 62 kpc, respectively [98,298]. The proximity enables spatially resolved studies of the SNRs, and the accurately known distances permit the analysis of the energetics of each SNR. Observations of the entire SNR population in a galaxy on the other hand allow us to study the physics of SNRs, their progenitors, and the impact of the environment of SNRs on their evolution. A luminosity distribution of the SNRs in each galaxy can be constructed, which reveals the cause for the systematic offsets and slope differences between different galaxies, most likely caused by different overall abundances, average ISM densities, or typical explosion energies, in addition to selection effects. In addition, observations of the SNRs in the LMC and the SMC allow us to study not only the global properties of SNRs in a galaxy, but also specific sub-classes in detail (e.g., sorted by X-ray and radio morphology, diameter, or progenitor supernova type).

Taking advantage of the high sensitivity of XMM-Newton expecially in the softer band, a survey of SNRs and candidates in the Magellanic Clouds (MCs) has been performed with XMM-Newton [e.g.,

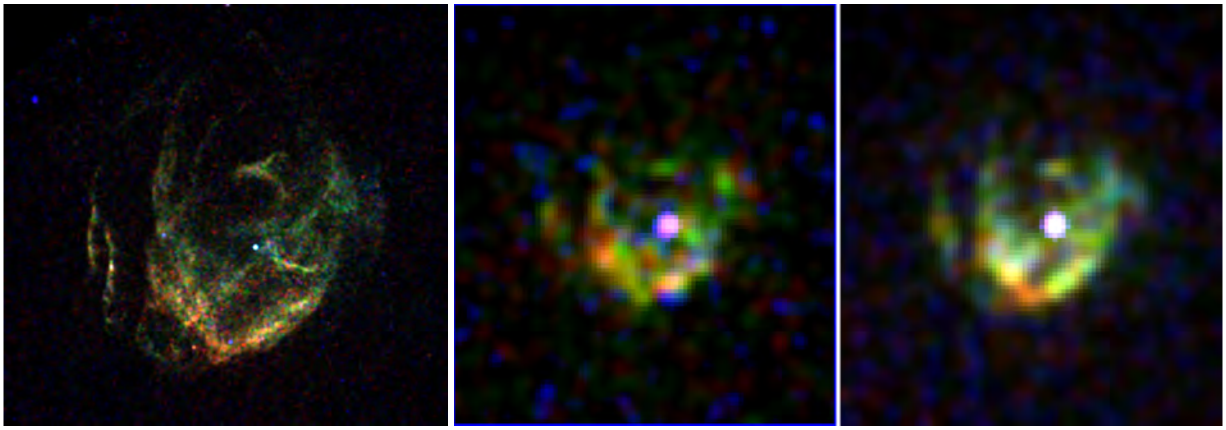

Figure 27. Left: Chandra observation of the Galactic SNR Kes 79 with a CCO (red: 0.5 – 1.2 keV, green: 1.2 – 2.0 keV, blue: 2.0 – 7.0 keV). Middle: Image from a SIXTE simulation of an AXIS observation of Kes 79 assuming LMC distance and an exposure of 10 ks. Right: Same as in the middle image but for 50 ks.

158,159,180,181]. In these studies, a new pulsar wind nebulae or an X-ray binary in an SNR were discovered (e.g., LMC SNR J0453-6829 [107], LMC SNR J0513-6724 [182], SMC SNR DEM S5 [7]).

AXIS will allow us to continue the studies of the SNR populations in the MC started with XMM-Newton, with significantly improved spatial resolution and sensitivity. It will allow us to study each of the SNRs in great detail by resolving interior structures, and also detecting NSs formed in the supernova. As CCOs and AXPs are fainter X-ray sources with luminosities of $L_X = 10^{32-36}$ erg s^{-1} (in comparison to XRBs, which are typically brighter $L_X \geq 10^{37}$ erg s^{-1}, not many NSs inside SNRs have been detected yet. The resolution and sensitivity of AXIS will allow us to resolve a CCO even at the distance of the MCs (see Fig. 27).

9. Outflows from binaries

9.1. Microquasar jets

Microquasars are minature versions of quasars, believed to host a central black hole surrounded by an accretion disk, and emitting relativistic jets that are very similar to those found in active galaxies. These jets offer an exciting probe of outflows from black holes and their feedback on the interstellar and intergalactic medium. Microquasar jets studies further provides a zoomed-in version of the large scale jets from quasars. The study of their dynamical evolution is possible on timescales that are inaccessible for active galactic nuclei jets.

We so far know of radio/X-ray jets in five microquasars, and thanks to Chandra's imaging resolution, these jets have been resolved into knots of emisison that trace the ejection and particle acceleration process. The broadband spectrum of some of these is consistent with synchrotron emission from high-energy (up to 10 TeV) particles that were accelerated in the shock waves formed within the relativistic ejecta or by the interaction of the jets with the ISM. However often, the nature of the spectrum or scale size of the knots can not be confirmed given the poor count statistics or the decline of the PSF off-axis. AXIS's unprecedented sensitivity and PSF over a large field of view will provide a leap in such studies and help discover new compact and large scale jets from a variety of accretion-powered sources.

One notable source known to power both short- and large-scale X-ray jets is the microquasar SS 433 powering the radio lobes of the large diffuse nebula, W50. An X-ray observational campaign has led to the discovery of knots of hard x-ray emission that soften as we move away from SS 433 towards the large scale lobes marking the site of the interaction between the jets and the ambient medium or SNR shell. Upon examining the Chandra and XMM-Newton data of this source, we find evidence for these knots, located at $\geq$30 pc away from SS 433, to be moving; however with a large uncertainty. One of these knots marks the site of particle re-acceleration to energies up to a few 100 TeV, through a yet poorly understood mechanism. In Fig 28, we show how AXIS will enable an accurate measurement of the velocity. This will in turn address the physics of particle acceleration or deceleration as the jet encounters the surrounding medium (see [259] for a recent study).

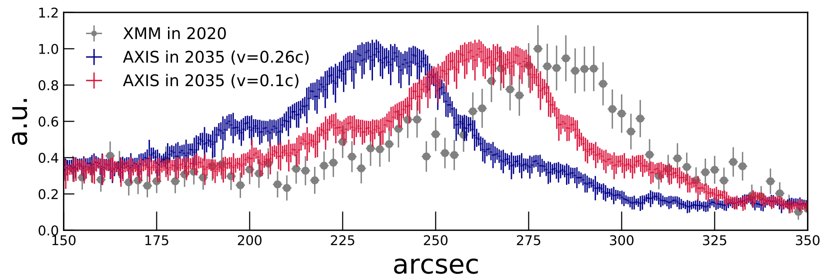

Figure 28. This figure illustrates the need for AXIS to follow the proper motion of microquasar jets (SS 433/W50 in this special case) while taking advantage of the legacy of Chandra and XMM-Newton observations of such outflows.

9.2. Transient Outflows

When X-ray binaries undergo an outburst they can launch jets, typically observed at radio wavelengths. As these jet ejections fly away from the binary at mildly to highly relativistic speeds they eventually begin to interact with the ISM at late times, forming external shocks and accelerating particles, leading to a brightening in X-rays. These outflows are often large ($\sim 10''$) and relatively faint (see Figure 29), thus many can only be studied with AXIS due to its high sensitivity and exquisite angular resolution. Jet ejections from several BH X-ray binaries have been observed by Chandra [57,58,76,145,190]. Studying the late time deceleration and X-ray emission from these jets can help us to place tight constraints on their energetics, and therefore, possible launching mechanisms.

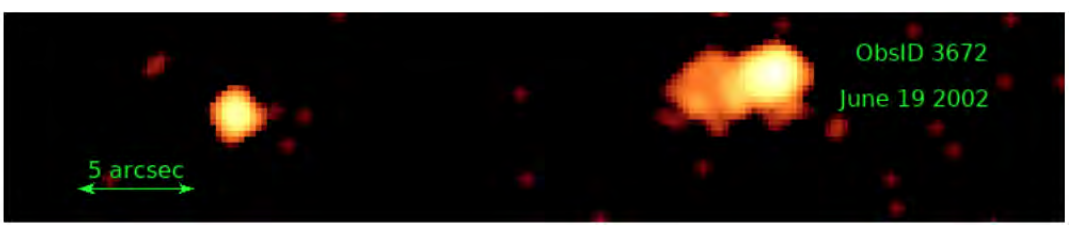

Figure 29. Chandra ACIS observations of the X-ray emitting jets launched by XTE J1550-564. The jet is the extended X-ray emission seen on the right side of the figure, while the binary is the X-ray source on the left. Figure adopted from [190] and modified.

Other X-ray binaries have also showed mildly relativistic outflows. For example, Chandra has observed X-ray emitting clumps being launched from the high mass gamma-ray binary LS 2883/PSR B1259-63, which move at velocities of $\approx 0.1c$ and show signs of being accelerated [115,117,152,222,223]. This material is thought to be debris from the massive companion's stellar disk, which is inclined to the orbit of the pulsar such that the pulsar passes through it twice each orbit. When the pulsar passes through the disk some of this material is ejected from the binary, and then is shocked and accelerated by its interaction with the pulsar wind (see [24,223] for a more detailed explanation). To date, this remains the only high-mass gamma-ray binary to show such phenomena, though it has been searched for in others (see e.g., [150,214]). Chandra has played a pivotal role in the discovery and follow-up of transient outflows from a wide array of different types of binaries. AXIS is the only observatory in the near future with sufficient sensitivity and angular resolution to allow for the continuation of these types of studies.

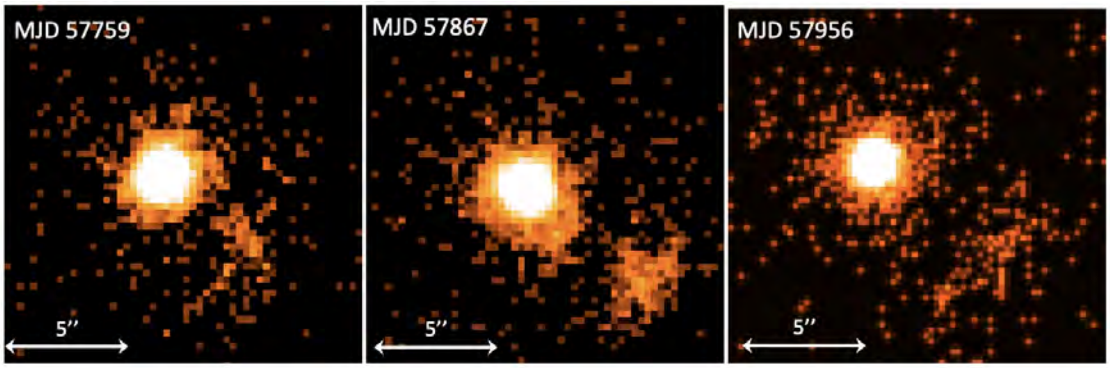

Figure 30. Chandra ACIS observations of the X-ray emitting clump launched from the high mass gamma-ray binary PSR B1259-63. The clump showed signs of acceleration and reached a velocity of $\approx 0.1c$ (see [115] for additional details).

10. Conclusions

AXIS is best for compact objects and SNR science!

1. Abazajian, K. N. 2011, , 2011, 010
2. Abbasi, R., Ackermann, M., Adams, J., et al. 2022, ApJ, 930, L24
3. —. 2023, arXiv e-prints, arXiv:2307.07576
4. Abbott, R., Abbott, T. D., Acernese, F., et al. 2023, Physical Review X, 13, 011048
5. Ackermann, M., Ajello, M., Albert, A., et al. 2017, ApJ, 840, 43
6. Alford, J. A. J., & Halpern, J. P. 2023, ApJ, 944, 36
7. Alsaberi, R. Z. E., Maitra, C., Filipović, M. D., et al. 2019, MNRAS, 486, 2507
8. An, H., & Archibald, R. 2019, ApJ, 877, L10
9. An, H., Cumming, A., & Kaspi, V. M. 2018, ApJ, 859, 16
10. An, H., Kaspi, V. M., Tomsick, J. A., et al. 2012, ApJ, 757, 68
11. An, H., Kaspi, V. M., Beloborodov, A. M., et al. 2014, ApJ, 790, 60
12. Anastasopoulou, K., Ponti, G., Sormani, M. C., et al. 2023, A&A, 671, A55
13. Andrés, A., van den Eijnden, J., Degenaar, N., et al. 2022, MNRAS, 510, 2851
14. Antonini, F., & Gieles, M. 2020, Ph. Rev. D, 102, 123016
15. Antonini, F., Gieles, M., Dosopoulou, F., & Chattopadhyay, D. 2023, MNRAS, 522, 466
16. Arnaud, K. A. 1996, in Astronomical Society of the Pacific Conference Series, Vol. 101, Astronomical Data Analysis Software and Systems V, ed. G. H. Jacoby & J. Barnes, 17
17. Bachetti, M., Harrison, F. A., Walton, D. J., et al. 2014, Nature, 514, 202
18. Baganoff, F. K., Bautz, M. W., Brandt, W. N., et al. 2001, Nature, 413, 45
19. Baganoff, F. K., Maeda, Y., Morris, M., et al. 2003, ApJ, 591, 891
20. Bahramian, A., Heinke, C. O., Tudor, V., et al. 2017, MNRAS, 467, 2199
21. —. 2017, MNRAS, 467, 2199
22. Bahramian, A., Tremou, E., Tetarenko, A. J., et al. 2023, ApJ, 948, L7

23. Bandiera, R. 2008, A&A, 490, L3
24. Barkov, M. V., & Bosch-Ramon, V. 2016, MNRAS, 456, L64
25. Barkov, M. V., Lyutikov, M., Klingler, N., & Bordas, P. 2019, MNRAS, 485, 2041
26. Beloborodov, A. M. 2009, ApJ, 703, 1044
27. Bisnovatyi-Kogan, G. S. 1993, Astronomical and Astrophysical Transactions, 3, 287
28. Bogdanov, S., Bahramian, A., Heinke, C. O., et al. 2021, ApJ, 912, 124
29. Bogdanov, S., Grindlay, J. E., Heinke, C. O., et al. 2006, ApJ, 646, 1104
30. Bogdanov, S., Heinke, C. O., Özel, F., & Güver, T. 2016, ApJ, 831, 184
31. Bogdanov, S., Ho, W. C. G., Enoto, T., et al. 2019, ApJ, 877, 69
32. Borkowski, K. J., Hendrick, S. P., & Reynolds, S. P. 2006, ApJ, 652, 1259
33. Bortolas, E., Mapelli, M., & Spera, M. 2017, MNRAS, 469, 1510
34. Boyce, H., Haggard, D., Witzel, G., et al. 2019, ApJ, 871, 161
35. —. 2022, ApJ, 931, 7
36. Bühler, R., & Giomi, M. 2016, MNRAS, 462, 2762
37. Bykov, A. M., Ellison, D. C., Osipov, S. M., & Vladimirov, A. E. 2014, ApJ, 789, 137
38. Calderón, D., Cuadra, J., Schartmann, M., Burkert, A., & Russell, C. M. P. 2020, ApJ, 888, L2
39. Capelli, R., Warwick, R. S., Porquet, D., Gillessen, S., & Predehl, P. 2011, A&A, 530, A38
40. —. 2012, A&A, 545, A35
41. Carpano, S., Haberl, F., Maitra, C., & Vasilopoulos, G. 2018, MNRAS, 476, L45
42. Carretti, E., Crocker, R. M., Staveley-Smith, L., et al. 2013, Nature, 493, 66
43. Cassisi, S., Iben, Icko, J., & Tornambè, A. 1998, ApJ, 496, 376
44. Catuneanu, A., Heinke, C. O., Sivakoff, G. R., Ho, W. C. G., & Servillat, M. 2013, ApJ, 764, 145
45. Cerutti, B., Philippov, A. A., & Spitkovsky, A. 2016, MNRAS, 457, 2401
46. Chawla, N. V., Bowyer, K. W., Hall, L. O., & Kegelmeyer, W. P. 2011, arXiv e-prints, arXiv:1106.1813
47. Chen, H.-L., Woods, T. E., Yungelson, L. R., et al. 2019, MNRAS, 490, 1678
48. Chen, S., Kargaltsev, O., Yang, H., et al. 2023, ApJ, 948, 59
49. Chomiuk, L., Strader, J., Maccarone, T. J., et al. 2013, ApJ, 777, 69
50. Chuard, D., Terrier, R., Goldwurm, A., et al. 2018, A&A, 610, A34
51. Churazov, E., Khabibullin, I., Sunyaev, R., & Ponti, G. 2017, MNRAS, 471, 3293
52. Churchwell, E., Babler, B. L., Meade, M. R., et al. 2009, PASP, 121, 213
53. Ciurlo, A., Campbell, R. D., Morris, M. R., et al. 2023, ApJ, 944, 136
54. Clark, G. W. 1975, ApJ, 199, L143
55. Clavel, M., Terrier, R., Goldwurm, A., et al. 2013, A&A, 558, A32
56. Colbert, E. J. M., & Mushotzky, R. F. 1999, ApJ, 519, 89
57. Corbel, S., Fender, R. P., Tzioumis, A. K., et al. 2002, Science, 298, 196
58. Corbel, S., Kaaret, P., Fender, R. P., et al. 2005, ApJ, 632, 504
59. Côte, P., Scott, A., Balogh, M., et al. 2012, in Society of Photo-Optical Instrumentation Engineers (SPIE) Conference Series, Vol. 8442, Space Telescopes and Instrumentation 2012: Optical, Infrared, and Millimeter Wave, ed. M. C. Clampin, G. G. Fazio, H. A. MacEwen, & J. Oschmann, Jacobus M., 844215
60. Cuadra, J., Nayakshin, S., & Martins, F. 2008, MNRAS, 383, 458
61. Cuadra, J., Nayakshin, S., Springel, V., & Di Matteo, T. 2005, MNRAS, 360, L55
62. Dauser, T., Middleton, M., & Wilms, J. 2017, MNRAS, 466, 2236
63. De Luca, A. 2017, in Journal of Physics Conference Series, Vol. 932, Journal of Physics Conference Series, 012006
64. Degenaar, N., Wijnands, R., Cackett, E. M., et al. 2012, A&A, 545, A49
65. Degenaar, N., Wijnands, R., Bahramian, A., et al. 2015, MNRAS, 451, 2071
66. Deibel, A., Cumming, A., Brown, E. F., & Reddy, S. 2017, ApJ, 839, 95
67. Denissenkov, P. A., Herwig, F., Woodward, P., et al. 2019, MNRAS, 488, 4258
68. Dexter, J., Agol, E., & Fragile, P. C. 2009, ApJ, 703, L142
69. Dexter, J., & O'Leary, R. M. 2014, ApJ, 783, L7

70. Di Mauro, M., & Winkler, M. W. 2021, Ph. Rev. D, 103, 123005
71. Dodds-Eden, K., Sharma, P., Quataert, E., et al. 2010, ApJ, 725, 450
72. Dodds-Eden, K., Porquet, D., Trap, G., et al. 2009, ApJ, 698, 676
73. Eckart, A., Baganoff, F. K., Morris, M., et al. 2004, A&A, 427, 1
74. Eckart, A., Baganoff, F. K., Schödel, R., et al. 2006, A&A, 450, 535
75. Eckart, A., García-Marín, M., Vogel, S. N., et al. 2012, A&A, 537, A52
76. Espinasse, M., Corbel, S., Kaaret, P., et al. 2020, ApJ, 895, L31
77. Event Horizon Telescope Collaboration, Akiyama, K., Alberdi, A., et al. 2022, ApJ, 930, L12
78. —. 2022, ApJ, 930, L13
79. Fazio, G. G., Hora, J. L., Witzel, G., et al. 2018, ApJ, 864, 58
80. Ferrand, G., & Safi-Harb, S. 2012, Advances in Space Research, 49, 1313
81. Ferrand, G., Tanikawa, A., Warren, D. C., et al. 2022, ApJ, 930, 92
82. Fornasini, F. M., Tomsick, J. A., Bodaghee, A., et al. 2014, ApJ, 796, 105
83. Freitag, M., Amaro-Seoane, P., & Kalogera, V. 2006, ApJ, 649, 91
84. Fritz, T. K., Chatzopoulos, S., Gerhard, O., et al. 2016, ApJ, 821, 44
85. Fürst, F., Walton, D. J., Harrison, F. A., et al. 2016, ApJ, 831, L14
86. Gaensler, B. M., & Slane, P. O. 2006, ARA&A, 44, 17
87. Gallego-Cano, E., Schödel, R., Nogueras-Lara, F., et al. 2020, A&A, 634, A71
88. Gavriil, F. P., Dib, R., & Kaspi, V. M. 2008, in American Institute of Physics Conference Series, Vol. 983, 40 Years of Pulsars: Millisecond Pulsars, Magnetars and More, ed. C. Bassa, Z. Wang, A. Cumming, & V. M. Kaspi, 234
89. Gavriil, F. P., Gonzalez, M. E., Gotthelf, E. V., et al. 2008, Science, 319, 1802
90. Gehrz, R. D., Truran, J. W., Williams, R. E., & Starrfield, S. 1998, PASP, 110, 3
91. Generozov, A., Stone, N. C., Metzger, B. D., & Ostriker, J. P. 2018, MNRAS, 478, 4030
92. Genzel, R. 2022, Reviews of Modern Physics, 94, 020501
93. Genzel, R., Eisenhauer, F., & Gillessen, S. 2010, Reviews of Modern Physics, 82, 3121
94. Gessner, A., & Janka, H.-T. 2018, ApJ, 865, 61, arXiv:1802.05274 [astro-ph, physics:hep-ph]
95. Giardino, G., Pillitteri, I., Favata, F., & Micela, G. 2008, A&A, 490, 113
96. Gonthier, P. L., Harding, A. K., Ferrara, E. C., et al. 2018, ApJ, 863, 199
97. Gotthelf, E. V., Halpern, J. P., & Alford, J. 2013, ApJ, 765, 58
98. Graczyk, D., Pietrzyński, G., Thompson, I. B., et al. 2014, ApJ, 780, 59
99. GRAVITY Collaboration, Abuter, R., Amorim, A., et al. 2018, A&A, 615, L15
100. —. 2020, A&A, 636, L5
101. Gravity+ Collaboration, Abuter, R., Alarcon, P., et al. 2022, The Messenger, 189, 17
102. Greiner, J. 1996, Supersoft X-Ray Sources, Vol. 472
103. —. 2000, New A, 5, 137
104. Guest, B. T., & Safi-Harb, S. 2020, MNRAS, 498, 821
105. Guillot, S., Servillat, M., Webb, N. A., & Rutledge, R. E. 2013, ApJ, 772, 7
106. Gúrpide, A., Godet, O., Vasilopoulos, G., Webb, N. A., & Olive, J. F. 2021, A&A, 654, A10
107. Haberl, F., Filipović, M. D., Bozzetto, L. M., et al. 2012, A&A, 543, A154
108. Hachisu, I., Kato, M., & Nomoto, K. 1999, ApJ, 522, 487
109. Haggard, D., Cool, A. M., & Davies, M. B. 2009, ApJ, 697, 224
110. Haggard, D., Nynka, M., Mon, B., et al. 2019, ApJ, 886, 96
111. Hailey, C. J., Mori, K., Bauer, F. E., et al. 2018, Nature, 556, 70
112. —. 2018, Nature, 556, 70
113. Hailey, C. J., Mori, K., Perez, K., et al. 2016, ApJ, 826, 160
114. Harding, A. K. 2013, Frontiers of Physics, 8, 679
115. Hare, J., Kargaltsev, O., Pavlov, G., & Beniamini, P. 2019, ApJ, 882, 74
116. Hare, J., Kargaltsev, O., & Rangelov, B. 2018, ApJ, 865, 33

117. Hare, J., Pavlov, G. G., Kargaltsev, O., & Garmire, G. P. 2023, Research Notes of the American Astronomical Society, 7, 52
118. Hare, J., Yang, H., Kargaltsev, O., et al. 2021, The Astronomer's Telegram, 14499, 1
119. Hebbar, P. R., & Heinke, C. O. 2023, ApJ, 949, 12
120. Heinke, C. O., Edmonds, P. D., Grindlay, J. E., et al. 2003, ApJ, 590, 809
121. Heinke, C. O., Grindlay, J. E., Edmonds, P. D., et al. 2005, ApJ, 625, 796
122. —. 2003, ApJ, 598, 516
123. Heinke, C. O., Grindlay, J. E., Lugger, P. M., et al. 2003, ApJ, 598, 501
124. Heinke, C. O., Wijnands, R., Cohn, H. N., et al. 2006, ApJ, 651, 1098
125. Heywood, I., Rammala, I., Camilo, F., et al. 2022, ApJ, 925, 165
126. —. 2022, ApJ, 925, 165
127. Ho, W. C. G. 2011, MNRAS, 414, 2567
128. —. 2013, MNRAS, 429, 113
129. Ho, W. C. G., Zhao, Y., Heinke, C. O., et al. 2021, MNRAS, 506, 5015
130. Hobbs, G., Lorimer, D. R., Lyne, A. G., & Kramer, M. 2005, MNRAS, 360, 974
131. Holland-Ashford, T., Lopez, L. A., Auchettl, K., Temim, T., & Ramirez-Ruiz, E. 2017, ApJ, 844, 84
132. Hong, J., van den Berg, M., Grindlay, J. E., Servillat, M., & Zhao, P. 2012, ApJ, 746, 165
133. Hong, J. S., van den Berg, M., Grindlay, J. E., & Laycock, S. 2009, ApJ, 706, 223
134. Hooper, D., & Goodenough, L. 2011, Physics Letters B, 697, 412
135. Horowitz, C. J., Berry, D. K., Briggs, C. M., et al. 2015, Phys. Rev. Lett., 114, 031102
136. Ibrahim, A. I., Safi-Harb, S., Swank, J. H., et al. 2002, ApJ, 574, L51
137. Icecube Collaboration, Abbasi, R., Ackermann, M., et al. 2023, Science, 380, 1338
138. Igoshev, A. P., Chruslinska, M., Dorozsmai, A., & Toonen, S. 2021, MNRAS, 508, 3345, aDS Bibcode: 2021MNRAS.508.3345I
139. Israel, G. L., Belfiore, A., Stella, L., et al. 2017, Science, 355, 817
140. Janka, H. T., & Mueller, E. 1994, A&A, 290, 496
141. Jawor, J. A., & Tauris, T. M. 2022, MNRAS, 509, 634
142. Johnson, M. D., Akiyama, K., Blackburn, L., et al. 2023, Galaxies, 11, 61
143. Jonker, P. G., Bassa, C. G., Nelemans, G., et al. 2011, ApJS, 194, 18
144. Jonker, P. G., Torres, M. A. P., Hynes, R. I., et al. 2014, ApJS, 210, 18
145. Kaaret, P., Corbel, S., Tomsick, J. A., et al. 2003, ApJ, 582, 945
146. Kahabka, P., & van den Heuvel, E. P. J. 1997, ARA&A, 35, 69
147. Kaplan, D. L. 2008, in American Institute of Physics Conference Series, Vol. 968, Astrophysics of Compact Objects, ed. Y.-F. Yuan, X.-D. Li, & D. Lai, 129
148. Kargaltsev, O., Cerutti, B., Lyubarsky, Y., & Striani, E. 2015, Space Sci. Rev., 191, 391
149. Kargaltsev, O., Klingler, N., Chastain, S., & Pavlov, G. G. 2017, in Journal of Physics Conference Series, Vol. 932, Journal of Physics Conference Series, 012050
150. Kargaltsev, O., Klingler, N. J., Hare, J., & Volkov, I. 2022, ApJ, 925, 20
151. Kargaltsev, O., & Pavlov, G. G. 2008, in American Institute of Physics Conference Series, Vol. 983, 40 Years of Pulsars: Millisecond Pulsars, Magnetars and More, ed. C. Bassa, Z. Wang, A. Cumming, & V. M. Kaspi, 171
152. Kargaltsev, O., Pavlov, G. G., Durant, M., Volkov, I., & Hare, J. 2014, ApJ, 784, 124
153. Kargaltsev, O., Pavlov, G. G., Klingler, N., & Rangelov, B. 2017, ArXiv e-prints, arXiv:1708.00456 [astro-ph.HE]
154. Kaspi, V. M. 2010, Proceedings of the National Academy of Science, 107, 7147
155. Kaspi, V. M., & Beloborodov, A. M. 2017, ARA&A, 55, 261
156. Kaspi, V. M., Gavriil, F. P., Woods, P. M., et al. 2003, ApJ, 588, L93
157. Katsuda, S., Morii, M., Janka, H.-T., et al. 2018, ApJ, 856, 18
158. Kavanagh, P. J., Sasaki, M., Filipović, M. D., et al. 2022, MNRAS, 515, 4099
159. Kavanagh, P. J., Sasaki, M., Bozzetto, L. M., et al. 2016, A&A, 586, A4
160. Khabibullin, I., Churazov, E., & Sunyaev, R. 2022, MNRAS, 509, 6068

161. Kilgard, R. E., Cowan, J. J., Garcia, M. R., et al. 2005, ApJS, 159, 214
162. King, A., Lasota, J.-P., & Middleton, M. 2023, New A Rev., 96, 101672
163. Kırmızıbayrak, D., & Heyl, J. 2023, IAU Symposium, 363, 318
164. Kirsten, F., Marcote, B., Nimmo, K., et al. 2022, Nature, 602, 585
165. Koliopanos, F., Vasilopoulos, G., Godet, O., et al. 2017, A&A, 608, A47
166. Kollmeier, J. A., Zasowski, G., Rix, H.-W., et al. 2017, arXiv e-prints, arXiv:1711.03234
167. Kong, A. K. H., Hu, C.-P., Lin, L. C.-C., et al. 2016, MNRAS, 461, 4395
168. Kouveliotou, C., Eichler, D., Woods, P. M., et al. 2003, ApJ, 596, L79
169. Kovlakas, K., Zezas, A., Andrews, J. J., et al. 2020, MNRAS, 498, 4790
170. Koyama, K., Takikawa, Y., Hyodo, Y., et al. 2009, , 61, S255
171. Krivonos, R., Hailey, C., Mori, K., et al. 2021, in Astronomical Society of the Pacific Conference Series, Vol. 528, New Horizons in Galactic Center Astronomy and Beyond, ed. M. Tsuboi & T. Oka, 139
172. Kuiper, L., Hermsen, W., den Hartog, P. R., & Collmar, W. 2006, ApJ, 645, 556
173. Lee, J. C., Whitmore, B. C., Thilker, D. A., et al. 2022, ApJS, 258, 10
174. Li, Y.-P., Yuan, F., & Wang, Q. D. 2017, MNRAS, 468, 2552
175. Licquia, T. C., & Newman, J. A. 2015, ApJ, 806, 96
176. Lin, L. C.-C., Hu, C.-P., Kong, A. K. H., et al. 2015, MNRAS, 454, 1644
177. Lin, L. C.-C., Hu, C.-P., Li, K.-L., et al. 2020, MNRAS, 491, 5682
178. Liotine, C., Zevin, M., Berry, C. P. L., Doctor, Z., & Kalogera, V. 2023, ApJ, 946, 4
179. Maccarone, T. J., Degenaar, N., Tetarenko, B. E., et al. 2022, MNRAS, 512, 2365
180. Maggi, P., Haberl, F., Kavanagh, P. J., et al. 2016, A&A, 585, A162
181. Maggi, P., Filipović, M. D., Vukotić, B., et al. 2019, A&A, 631, A127
182. Maitra, C., Haberl, F., Filipović, M. D., et al. 2019, MNRAS, 490, 5494
183. Mallick, L., & Dewangan, G. C. 2018, ApJ, 863, 178
184. Maoz, D., Hallakoun, N., & Badenes, C. 2018, MNRAS, 476, 2584
185. Marin, F., Churazov, E., Khabibullin, I., et al. 2023, Nature, 619, 41
186. Markoff, S., Falcke, H., Yuan, F., & Biermann, P. L. 2001, A&A, 379, L13
187. Mereghetti, S., Pons, J. A., & Melatos, A. 2015, Space Sci. Rev., 191, 315
188. Merritt, D. 2010, ApJ, 718, 739
189. Middleton, M., Gúrpide, A., & Walton, D. J. 2023, MNRAS, 519, 2224
190. Migliori, G., Corbel, S., Tomsick, J. A., et al. 2017, MNRAS, 472, 141
191. Miller-Jones, J. C. A., Strader, J., Heinke, C. O., et al. 2015, MNRAS, 453, 3918
192. Miller-Jones, J. C. A., Deller, A. T., Shannon, R. M., et al. 2018, MNRAS, 479, 4849
193. Miralda-Escudé, J., & Gould, A. 2000, ApJ, 545, 847
194. Mong, Y. L., & Ng, C. Y. 2018, ApJ, 852, 86
195. Mori, K., Mandel, S., Hailey, C. J., et al. 2022, arXiv e-prints, arXiv:2204.09812
196. Mori, K., Hailey, C. J., Schutt, T. Y. E., et al. 2021, ApJ, 921, 148
197. —. 2021, ApJ, 921, 148
198. Morris, M. 1993, ApJ, 408, 496
199. Morris, M. R. 2023, arXiv e-prints, arXiv:2302.02431
200. Mossoux, E., Finociety, B., Beckers, J. M., & Vincent, F. H. 2020, A&A, 636, A25
201. Muno, M. P., Pfahl, E., Baganoff, F. K., et al. 2005, ApJ, 622, L113
202. Muno, M. P., Baganoff, F. K., Bautz, M. W., et al. 2004, ApJ, 613, 326
203. —. 2004, ApJ, 613, 326
204. Muno, M. P., Clark, J. S., Crowther, P. A., et al. 2006, ApJ, 636, L41
205. Muno, M. P., Bauer, F. E., Baganoff, F. K., et al. 2009, ApJS, 181, 110
206. —. 2009, ApJS, 181, 110
207. Nakashima, S., Koyama, K., Wang, Q. D., & Enokiya, R. 2019, ApJ, 875, 32

208. National Academies of Sciences, E., & Medicine. 2021, Pathways to Discovery in Astronomy and Astrophysics for the 2020s
209. Neilsen, J., Nowak, M. A., Gammie, C., et al. 2013, ApJ, 774, 42
210. Neilsen, J., Markoff, S., Nowak, M. A., et al. 2015, ApJ, 799, 199
211. Ness, J. U., Beardmore, A. P., Osborne, J. P., et al. 2015, A&A, 578, A39
212. Ng, C. Y., & Romani, R. W. 2004, ApJ, 601, 479
213. —. 2008, ApJ, 673, 411
214. Ng, C. Y., Ho, W. C. G., Gotthelf, E. V., et al. 2019, ApJ, 880, 147
215. Niu, S., Xie, F.-G., Sun, W., & Ji, L. 2023, Research in Astronomy and Astrophysics, 23, 085005
216. Nowak, M. A., Neilsen, J., Markoff, S. B., et al. 2012, ApJ, 759, 95
217. Olausen, S. A., Zhu, W. W., Vogel, J. K., et al. 2013, ApJ, 764, 1
218. Olmi, B., & Bucciantini, N. 2019, MNRAS, 490, 3608
219. Ootes, L. S., Vats, S., Page, D., et al. 2019, MNRAS, 487, 1447
220. Page, D., Prakash, M., Lattimer, J. M., & Steiner, A. W. 2011, Phys. Rev. Lett., 106, 081101
221. Panamarev, T., Just, A., Spurzem, R., et al. 2019, MNRAS, 484, 3279
222. Pavlov, G. G., Chang, C., & Kargaltsev, O. 2011, ApJ, 730, 2
223. Pavlov, G. G., Hare, J., Kargaltsev, O., Rangelov, B., & Durant, M. 2015, ApJ, 806, 192
224. Perez, K., Krivonos, R., & Wik, D. R. 2019, ApJ, 884, 153
225. Perna, R., & Pons, J. A. 2011, ApJ, 727, L51
226. Pierbattista, M., Harding, A. K., Gonthier, P. L., & Grenier, I. A. 2016, A&A, 588, A137
227. Pike, S. N., Negoro, H., Tomsick, J. A., et al. 2022, ApJ, 927, 190
228. Piskunov, A. E., Schilbach, E., Kharchenko, N. V., Röser, S., & Scholz, R. D. 2007, A&A, 468, 151
229. —. 2008, A&A, 477, 165
230. Plucinsky, P. P., Bogdan, A., & Marshall, H. L. 2022, in Society of Photo-Optical Instrumentation Engineers (SPIE) Conference Series, Vol. 12181, Society of Photo-Optical Instrumentation Engineers (SPIE) Conference Series, ed. J.-W. A. den Herder, S. Nikzad, & K. Nakazawa, 121816X
231. Pons, J. A., Link, B., Miralles, J. A., & Geppert, U. 2007, Phys. Rev. Lett., 98, 071101
232. Pons, J. A., & Rea, N. 2012, ApJ, 750, L6
233. Pons, J. A., Viganò, D., & Rea, N. 2013, Nature Physics, 9, 431
234. Ponti, G., Morris, M. R., Churazov, E., Heywood, I., & Fender, R. P. 2021, A&A, 646, A66
235. Ponti, G., Terrier, R., Goldwurm, A., Belanger, G., & Trap, G. 2010, ApJ, 714, 732
236. Ponti, G., De Marco, B., Morris, M. R., et al. 2015, MNRAS, 454, 1525
237. Ponti, G., George, E., Scaringi, S., et al. 2017, MNRAS, 468, 2447
238. Ponti, G., Hofmann, F., Churazov, E., et al. 2019, Nature, 567, 347
239. —. 2019, Nature, 567, 347
240. Pooley, D., & Hut, P. 2006, ApJ, 646, L143
241. Pooley, D., Lewin, W. H. G., Verbunt, F., et al. 2002, ApJ, 573, 184
242. Pooley, D., Lewin, W. H. G., Anderson, S. F., et al. 2003, ApJ, 591, L131
243. Posselt, B., & Pavlov, G. G. 2022, ApJ, 932, 83
244. Potekhin, A. Y., Zyuzin, D. A., Yakovlev, D. G., Beznogov, M. V., & Shibanov, Y. A. 2020, MNRAS, 496, 5052
245. Poutanen, J., Lipunova, G., Fabrika, S., Butkevich, A. G., & Abolmasov, P. 2007, MNRAS, 377, 1187
246. Predehl, P., Sunyaev, R. A., Becker, W., et al. 2020, Nature, 588, 227
247. Prialnik, D., & Kovetz, A. 1995, ApJ, 445, 789
248. Ransom, S. M., Hessels, J. W. T., Stairs, I. H., et al. 2005, Science, 307, 892
249. Rea, N., Israel, G. L., & Stella, L. 2004, Nuclear Physics B Proceedings Supplements, 132, 554
250. Rea, N., Israel, G. L., Pons, J. A., et al. 2013, ApJ, 770, 65
251. Ressler, S. M., White, C. J., & Quataert, E. 2023, MNRAS, 521, 4277
252. Revnivtsev, M., Sazonov, S., Churazov, E., et al. 2009, Nature, 458, 1142
253. Revnivtsev, M., Sazonov, S., Gilfanov, M., Churazov, E., & Sunyaev, R. 2006, A&A, 452, 169

254. Reynolds, S. P., Pavlov, G. G., Kargaltsev, O., et al. 2017, Space Sci. Rev., 207, 175
255. Rodríguez Castillo, G. A., Israel, G. L., Belfiore, A., et al. 2020, ApJ, 895, 60
256. Rogers, F., Zhang, S., Perez, K., Clavel, M., & Taylor, A. 2022, ApJ, 934, 19
257. Sacchi, A., Risaliti, G., & Miniutti, G. 2023, A&A, 671, A33
258. Safi-Harb, S. 2017, in Journal of Physics Conference Series, Vol. 932, Journal of Physics Conference Series, 012005
259. Safi-Harb, S., Mac Intyre, B., Zhang, S., et al. 2022, ApJ, 935, 163
260. Salvato, M., Buchner, J., Budavári, T., et al. 2018, MNRAS, 473, 4937
261. Sathyaprakash, R., Roberts, T. P., Walton, D. J., et al. 2019, MNRAS, 488, L35
262. Scholz, P., Kaspi, V. M., & Cumming, A. 2014, ApJ, 786, 62
263. Servillat, M., Dieball, A., Webb, N. A., et al. 2008, A&A, 490, 641
264. Shakura, N. I., & Sunyaev, R. A. 1973, A&A, 24, 337
265. Shannon, R. M., Johnston, S., & Manchester, R. N. 2014, MNRAS, 437, 3255
266. Shen, K. J., Boubert, D., Gänsicke, B. T., et al. 2018, ApJ, 865, 15
267. Shternin, P. S., Ofengeim, D. D., Heinke, C. O., & Ho, W. C. G. 2023, MNRAS, 518, 2775
268. Shternin, P. S., Yakovlev, D. G., Heinke, C. O., Ho, W. C. G., & Patnaude, D. J. 2011, MNRAS, 412, L108
269. Shu, X. W., Wang, T. G., Jiang, N., et al. 2017, ApJ, 837, 3
270. Siegert, T., Diehl, R., Khachatryan, G., et al. 2016, A&A, 586, A84
271. Siegert, T., Boggs, S. E., Tomsick, J. A., et al. 2020, ApJ, 897, 45
272. Slane, P., Helfand, D. J., van der Swaluw, E., & Murray, S. S. 2004, ApJ, 616, 403
273. Sofue, Y. 2023, MNRAS, 518, 6273
274. Solanki, S., Ressler, S. M., Murchikova, L., Stone, J. M., & Morris, M. R. 2023, ApJ, 953, 22
275. Soraisam, M. D., Gilfanov, M., Wolf, W. M., & Bildsten, L. 2016, MNRAS, 455, 668
276. Sridhar, N., & Metzger, B. D. 2022, ApJ, 937, 5
277. Sridhar, N., Metzger, B. D., Beniamini, P., et al. 2021, ApJ, 917, 13
278. Sridhar, N., Metzger, B. D., & Fang, K. 2022, arXiv e-prints, arXiv:2212.11236
279. Starrfield, S., Timmes, F. X., Hix, W. R., et al. 2004, ApJ, 612, L53
280. Stevenson, S., Willcox, R., Vigna-Gómez, A., & Broekgaarden, F. 2022, MNRAS, 513, 6105, aDS Bibcode: 2022MNRAS.513.6105S
281. Strader, J., Chomiuk, L., Maccarone, T. J., Miller-Jones, J. C. A., & Seth, A. C. 2012, Nature, 490, 71
282. Strader, J., Swihart, S., Chomiuk, L., et al. 2019, ApJ, 872, 42
283. Strohmayer, T. E., & Ibrahim, A. I. 2000, ApJ, 537, L111
284. Su, M., Slatyer, T. R., & Finkbeiner, D. P. 2010, ApJ, 724, 1044
285. —. 2010, ApJ, 724, 1044
286. Sun, L., Shu, X., & Wang, T. 2013, ApJ, 768, 167
287. Swihart, S. J., Strader, J., Chomiuk, L., et al. 2022, ApJ, 941, 199
288. The GRAVITY Collaboration, Abuter, R., Aimar, N., et al. 2023, arXiv e-prints, arXiv:2307.11821
289. Thompson, C., & Duncan, R. C. 1995, MNRAS, 275, 255
290. Tiengo, A., Esposito, P., Mereghetti, S., et al. 2013, Nature, 500, 312
291. —. 2013, Nature, 500, 312
292. Tranin, H., Godet, O., Webb, N., & Primorac, D. 2022, A&A, 657, A138
293. Türler, M., Chernyakova, M., Courvoisier, T. J. L., et al. 2010, A&A, 512, A49
294. Uchiyama, H., Nobukawa, M., Tsuru, T., Koyama, K., & Matsumoto, H. 2011, , 63, S903
295. Uchiyama, Y., Aharonian, F. A., Tanaka, T., Takahashi, T., & Maeda, Y. 2007, Nature, 449, 576
296. Valenti, E., Zoccali, M., Gonzalez, O. A., et al. 2016, A&A, 587, L6
297. van den Berg, M., Tagliaferri, G., Belloni, T., & Verbunt, F. 2004, A&A, 418, 509
298. van den Bergh, S. 1999, in New Views of the Magellanic Clouds, ed. Y. H. Chu, N. Suntzeff, J. Hesser, & D. Bohlender, Vol. 190, 569
299. van den Heuvel, E. P. J., Bhattacharya, D., Nomoto, K., & Rappaport, S. A. 1992, A&A, 262, 97
300. van der Meij, V., Guo, D., Kaper, L., & Renzo, M. 2021, A&A, 655, A31

301. Vasilopoulos, G., Haberl, F., Carpano, S., & Maitra, C. 2018, A&A, 620, L12
302. Vasilopoulos, G., Koliopanos, F., Haberl, F., et al. 2021, ApJ, 909, 50
303. Vasilopoulos, G., Koliopanos, F., Woods, T. E., et al. 2020, MNRAS, 499, 2007
304. Vats, S., & van den Berg, M. 2017, ApJ, 837, 130
305. Veena, V. S., Riquelme, D., Kim, W. J., et al. 2023, A&A, 674, L15
306. Viganò, D., Rea, N., Pons, J. A., et al. 2013, MNRAS, 434, 123
307. Vink, J., & Laming, J. M. 2003, ApJ, 584, 758
308. Walton, D. J., Mackenzie, A. D. A., Gully, H., et al. 2022, MNRAS, 509, 1587
309. Walton, D. J., Fürst, F., Heida, M., et al. 2018, ApJ, 856, 128
310. Wang, Q. D., Dong, H., & Lang, C. 2006, MNRAS, 371, 38
311. Wang, Q. D., Gotthelf, E. V., & Lang, C. C. 2002, Nature, 415, 148
312. Wang, Q. D., Li, J., Russell, C. M. P., & Cuadra, J. 2020, MNRAS, 492, 2481
313. Wang, Q. D., Nowak, M. A., Markoff, S. B., et al. 2013, Science, 341, 981
314. Watters, K. P., Romani, R. W., Weltevrede, P., & Johnston, S. 2009, ApJ, 695, 1289
315. Webb, N. A., Coriat, M., Traulsen, I., et al. 2020, A&A, 641, A136
316. Wijnands, R., Degenaar, N., & Page, D. 2017, Journal of Astrophysics and Astronomy, 38, 49
317. Witzel, G., Martinez, G., Willner, S. P., et al. 2021, ApJ, 917, 73
318. Wolf, W. M., Bildsten, L., Brooks, J., & Paxton, B. 2013, ApJ, 777, 136
319. Wolf, W. M., Townsend, R. H. D., & Bildsten, L. 2018, ApJ, 855, 127
320. Woods, T. E., Ghavamian, P., Badenes, C., & Gilfanov, M. 2017, Nature Astronomy, 1, 800
321. Woods, T. E., & Gilfanov, M. 2016, MNRAS, 455, 1770
322. Woosley, S. E. 1987, in The Origin and Evolution of Neutron Stars, ed. D. J. Helfand & J. H. Huang, Vol. 125, 255
323. Xu, X.-j., Wang, Q. D., & Li, X.-D. 2016, ApJ, 818, 136
324. Yang, H., Hare, J., Kargaltsev, O., et al. 2022, ApJ, 941, 104
325. Younes, G., Kouveliotou, C., & Roberts, O. 2016, GRB Coordinates Network, 19736, 1
326. Yuan, F., Quataert, E., & Narayan, R. 2003, ApJ, 598, 301
327. Yuasa, T., Makishima, K., & Nakazawa, K. 2012, ApJ, 753, 129
328. Yusef-Zadeh, F., Arendt, R. G., Wardle, M., & Heywood, I. 2023, ApJ, 949, L31
329. Yusef-Zadeh, F., Roberts, D., Wardle, M., Heinke, C. O., & Bower, G. C. 2006, ApJ, 650, 189
330. Yusef-Zadeh, F., Royster, M., Wardle, M., et al. 2020, MNRAS, 499, 3909
331. Zane, S., Haberl, F., Israel, G. L., et al. 2011, MNRAS, 410, 2428
332. Zevin, M., Samsing, J., Rodriguez, C., Haster, C.-J., & Ramirez-Ruiz, E. 2019, ApJ, 871, 91
333. Zhao, J., & Heinke, C. O. 2022, MNRAS, 511, 5964
334. —. 2022, MNRAS, 511, 5964
335. Zhu, W. W., Kaspi, V. M., McLaughlin, M. A., et al. 2011, ApJ, 734, 44
336. Zhu, Z., Li, Z., & Morris, M. R. 2018, ApJS, 235, 26
337. Zhu, Z., Li, Z., Morris, M. R., Zhang, S., & Liu, S. 2019, ApJ, 875, 44